

## A critical review of direct laser additive manufacturing ceramics

Dake Zhao<sup>1,2)</sup>, Guijun Bi<sup>1,2),✉</sup>, Jie Chen<sup>1,2)</sup>, WaiMeng Quach<sup>3)</sup>, Ran Feng<sup>4)</sup>, Antti Salminen<sup>5)</sup>, and Fangyong Niu<sup>6)</sup>

1) Institute of Intelligent Manufacturing, Guangdong Academy of Sciences, Guangzhou 510070, China

2) Guangdong Key Laboratory of Modern Control Technology, Guangzhou 510070, China

3) Department of Civil and Environmental Engineering, University of Macau, Macau 310058, China

4) School of Civil and Environmental Engineering, Harbin Institute of Technology, Shenzhen 518055, China

5) Department of Mechanical and Materials Engineering, Faculty of Technology, University of Turku, FI-20014 Turun yliopisto, Finland

6) Key Laboratory for Precision and Non-traditional Machining Technology of Ministry of Education, Dalian University of Technology, Dalian 116000, China

(Received: 3 April 2024; revised: 14 June 2024; accepted: 24 June 2024)

**Abstract:** The urgent need for integrated molding and sintering across various industries has inspired the development of additive manufacturing (AM) ceramics. Among the different AM technologies, direct laser additive manufacturing (DLAM) stands out as a group of highly promising technology for flexibly manufacturing ceramics without molds and adhesives in a single step. Over the last decade, significant and encouraging progress has been accomplished in DLAM of high-performance ceramics, including Al<sub>2</sub>O<sub>3</sub>, ZrO<sub>2</sub>, Al<sub>2</sub>O<sub>3</sub>/ZrO<sub>2</sub>, SiC, and others. However, high-performance ceramics fabricated by DLAM face challenges such as formation of pores and cracks and resultant low mechanical properties, hindering their practical application in high-end equipment. Further improvements are necessary before they can be widely adopted. Methods such as field-assisted techniques and post-processing can be employed to address these challenges, but a more systematic review is needed. This work aims to critically review the advancements in direct selective laser sintering/melting (SLS/SLM) and laser directed energy deposition (LDED) for various ceramic material systems. Additionally, it provides an overview of the current challenges, future research opportunities, and potential applications associated with DLAM of high-performance ceramics.

**Keywords:** 3D printing; laser additive manufacturing; ceramics; quality; microstructure; mechanical properties

## 1. Introduction

Diverse industries continuously favor high-performance ceramic parts for their exciting properties in extreme and severe environments, such as high temperatures resistance, outstanding corrosion and erosion resistance, and excellent wear resistance [1–2]. The substitution of superalloys with ceramics can objectively reduce the weight of critical core parts, promising to enhance the agility and maneuverability of aircraft [3–4]. Furthermore, the exceptional heat resistance of ceramics promotes combustion efficiency in internal combustion engines and turbomachinery, leading to reduced carbon emissions [5–6]. Ceramics also excel in handling the energy field, such as in the nuclear industry, where aggressive corrosion and high radiation fluxes are prevalent [7]. These high-value ceramic parts encompass exhaust nozzle, combustor liner, turbine blade, vane, molten salt reactor, catalytic converter, and electric vehicle bearing [8]. Therefore, the judicious utilization of ceramic parts is anticipated to achieve long-awaited goals of increased efficiency, enhanced performance, and extended lifespan of high-end

equipment. This is particularly pertinent given the rising emphasis on low emissions.

However, achieving the desired geometry and surface finish using conventional manufacturing processes to produce ceramic parts, such as shaping and sintering, involves multiple steps with long cycles, including material preparation, processing, sintering, heat treatment, and finishing [9–11]. In recent years, additive manufacturing (AM) has gained attention in the preparation of ceramics, metals, polymers, and other materials due to its flexible manufacturing method [12–15], providing an attractive solution for the preparation of high-performance ceramics, such as vat photopolymerization [16], digital light processing [17], and stereolithography [18]. Laser additive manufacturing (LAM), specifically referred to as direct laser additive manufacturing (DLAM) in this paper, provides the possibility for single-step shaping of complex near net shape ceramic parts, and generally have two main variants depending on the powder feeding mode: selective laser sintering/melting (SLS/SLM) and laser directed energy deposition (LDED). The SLM process correspond to laser powder bed fusion (LPBF) in the ISO 17296-2.

✉ Corresponding author: Guijun Bi Email: [gj.bi@giim.ac.cn](mailto:gj.bi@giim.ac.cn)

© University of Science and Technology Beijing 2024

The LDED process has been developed independently by different research teams around the world, giving rise to different acronymic terms, such as laser engineered net shaping (LENS), laser metal deposition (LMD), direct metal deposition (DMD), and directed laser deposition (DLD) [19]. In fabrication of a ceramic part by DLAM, a laser beam is used to transform the three dimensional (3D) design of the part into a complete solid in a rational manufacturing path. The ceramic parts are formed by sintering or solidifying in a layer-by-layer manner. As a result, these techniques demonstrate many advantages: (i) single-step moldless manufacturing of near-net shape ceramic parts; (ii) flexible design of structures and materials; (iii) low-volume and high-precision

production capabilities; (iv) easy fulfillment of quick-response and short-cycle manufacturing requirements. Research on the topics of ‘ceramic’ using the DLAM processes has attracted worldwide attention and investment over the last two decades, with the number of publications increasing over time, as illustrated in Fig. 1(a). The number of studies on the DLAM processes of critical topics for some typical ceramics during this period is shown in Fig. 1(b). It can be seen that the research involving  $\text{Al}_2\text{O}_3$  has received more attention. Moreover, a research report by SmarTech Analysis shows that the AM market for ceramics will reach 400 million USD by 2032 [20], further encouraging the careful study of high-performance ceramics by DLAM processes.

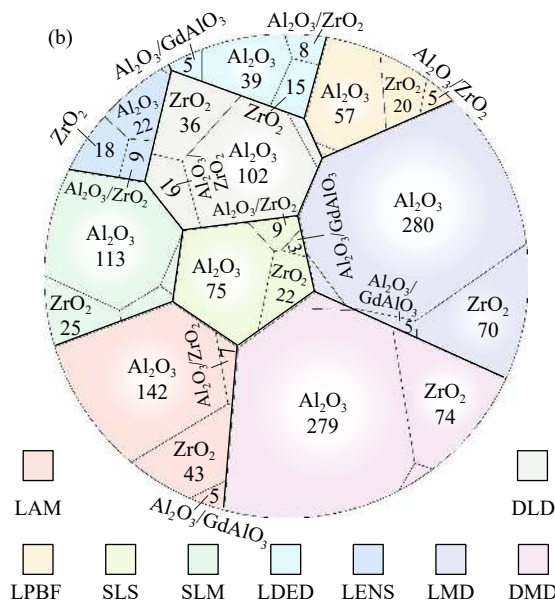
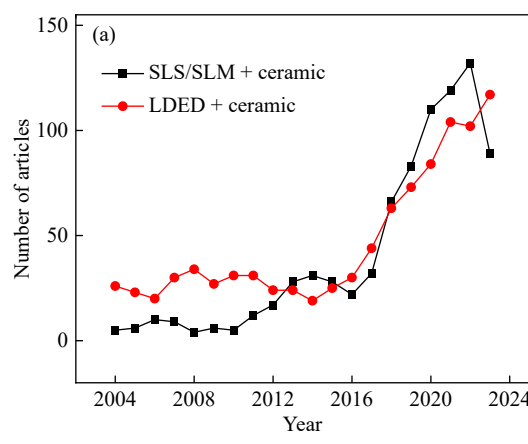


**Fig. 1.** Number of articles involved in ‘Core Collection Databases’ on ‘Web of Science’ with the topics of (a) ‘ceramic’ and ‘SLS/SLM’ or ‘LDED,’ as well as (b) the ‘LAM processes’ (abbreviated as ‘LAM,’ ‘LPBF,’ ‘SLS,’ ‘SLM,’ ‘LDED,’ ‘LENS,’ ‘LMD,’ ‘DMD,’ and ‘DLD’) and ‘typical ceramics’ (relate to ‘ $\text{Al}_2\text{O}_3$ ,’ ‘ $\text{ZrO}_2$ ,’ ‘ $\text{Al}_2\text{O}_3/\text{ZrO}_2$ ,’ and ‘ $\text{Al}_2\text{O}_3/\text{GdAlO}_3$ ’) till 31 December 2023.

The quality and properties are prerequisites for AMed ceramic parts to withstand various harsh conditions, typically influenced by multiple parameters of the DLAM processes within the domain-by-domain and layer-by-layer shaping characteristics. These parameters include laser power ( $P$ ), scanning speed ( $v$ ), closely linked to solidification rate ( $R$ ), powder bed density, powder feed rate ( $m$ ), scan pattern, hatch spacing (overlap rate), and processing atmosphere environment. The quality of DLAM ceramic parts encompasses defects, residual stresses, inclusions, geometric accuracy, and surface roughness, among others. The processing parameters significantly influence the shape and size of the smallest unit in continuous shaping part: a partial melting microfluid or a fully melted melt pool. The thermal and mass history of the DLAM process is complex and influenced by numerous parameters, which are the main factors for DLAM of high-quality parts. On one hand, regulating the thermal history homogenizes and refines the microstructure, guaranteeing material properties. On the other hand, efficient diffusion and convective transportation of matter (mass history), such as powder delivered to the melt pool and microfluid in

the melt pool, are essential for manufacturing low-defect high-precision parts. However, the multiple processing parameters and extremely high-temperature pose significant challenges to high-performance ceramic parts by controlling the thermal and mass history.

Several publications cover DLAM processes for high-performance ceramics [21–23]. However, as of this writing, there are few careful reviews of the parts quality for DLAM ceramics. The existing reviews on the correlation of defects, structures, and properties with process parameters need to be supplemented, especially the paucity of reviews dealing with the effects of external field-assisted shaping and post-treatment. Consequently, with a brief overview of the process principles (Section 2), this review article scrutinizes the progress in shaping quality (Section 3), microstructure (Section 4), and mechanical properties (Section 5) of DLAM ceramics, contributing positively to further academic research and potential industrial development. Furthermore, this review also prospects future opportunities and potential applications of DLAM high-quality ceramics, such as large-size, crack-free, high density, high accuracy, and high properties.

## 2. Process principles of DLAM ceramics

### 2.1. Selective laser sintering/melting

The selective laser sintering (SLS) process traces its origins to a patent filed by Carl R. Deckard in 1980, which outlined the fundamental principles of combining the SLS process with subsequent patents. In this process, the powder is initially spread flat on a powder bed and then subjected to a laser beam following a predefined trajectory. This is followed by downward movement of the powder bed to create a

layer. This sequence is repeated to realize the manufacturing of complex shape parts, as shown in Fig. 2(a). Similarly, the principle behind the selective laser melting (SLM) process is akin to the SLS process, with the distinction that the SLM process operates at temperatures exceeding the melting point of the additive material to produce dense parts. The SLM process originated as a research project at the Fraunhofer ILT in Aachen, Germany. Recent years have witnessed a gradual increase in research focused on SLM ceramics, driven by the demand for single-step processing of dense ceramics.

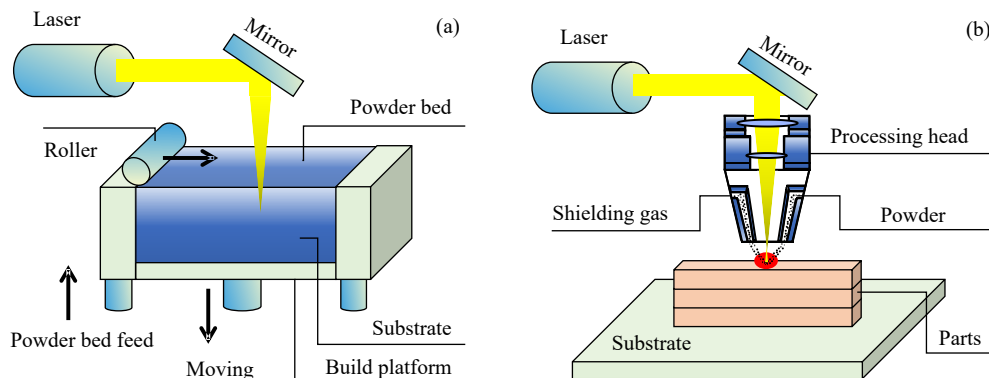


**Fig. 2.** Schematics of the direct laser additive manufacturing: (a) selective laser sintering/melting processes; (b) laser directed energy deposition process.

### 2.2. Laser directed energy deposition

LDED process synchronizes laser radiation and powder feeding, as shown in Fig. 2(b). This process involves converging spherical ceramic powders onto the substrate using a powder feeder and a nozzle. Simultaneously, a high-energy laser beam creates a melt pool on the substrate, melting the powders, followed by rapid cooling. By coordinating the rel-

ative movement between the processing head and the substrate according to a path pattern formed by layered slicing, a final 3D part can be fabricated. Various ceramic materials have been developed for single-step DLAM, as shown in Table 1, illustrating the significant potential of the DLAM processes (SLS/SLM and LDED) for the single-step manufacturing of high-quality advanced ceramics [5,24–51].

**Table 1.** Summary of main ceramic materials for the DLAM processes

Process	Ceramic materials
SLS/SLM	$\text{Al}_2\text{O}_3$ [24–25], $\text{ZrO}_2$ [26], $\text{SiC}$ [27], $\text{SiO}_2/\text{glass}$ [28], $\text{Y}_2\text{O}_3$ [29], $\text{BaTiO}_3$ [30], high-entropy carbide ceramics [31], $\text{Al}_2\text{O}_3/\text{ZrO}_2$ [32–34], $\text{Al}_2\text{O}_3/\text{GdAlO}_3$ [35], $\text{Al}_2\text{O}_3/\text{GdAlO}_3/\text{ZrO}_2$ [36]
LDED	$\text{Al}_2\text{O}_3$ [37–38], $\text{ZrO}_2$ [39], $\text{MgAl}_2\text{O}_4$ [40], mullite [41], $\text{Al}_2\text{O}_3/\text{ZrO}_2$ [42–47], $\text{Al}_2\text{O}_3/\text{Al}_2\text{TiO}_5$ [48], $\text{Al}_2\text{O}_3/\text{GdAlO}_3/\text{ZrO}_2$ [49], $\text{Al}_2\text{O}_3/\text{Y}_3\text{Al}_5\text{O}_{12}/\text{ZrO}_2$ [50], $\text{Al}_2\text{O}_3/\text{Y}_3\text{Al}_5\text{O}_{12}$ [51], $\text{Al}_2\text{O}_3/\text{mullite}$ [5]

## 3. Quality of DLAM ceramics

Manufacturing high-performance ceramic parts in a single step using the DLAM processes is not an effortless task, particularly when facing the urgent demands for large-size and crack-free. The DLAM physical process for ceramics is characterized by complexity and extremity due to the brittle nature and high melting point, encountering numerous processing variables. Hence, ensuring the quality of DLAM ceramics is an exciting and critical research topic. This section summarizes the geometric properties and surface roughness of ceramic parts fabricated by the DLAM processes. In addition, the defect inhibition methods are also reviewed carefully.

### 3.1. Geometric properties

Geometric dimensions and accuracy, direct indications of

the capability of the DLAM processes to fabricate high-performance ceramic parts, have been the focus of numerous studies. Table 2 provides a detailed summary of research on these factors [24–26,32–33,37–38,42,49,52–57]. The SLS/SLM processes, with solid sintering or partial melting features, are recognized for their ability to fabricate complex shape ceramics. However, they often yield low densities and surface roughness. For instance, the maximum transverse section dimensions (width) of SLS/SLM  $\text{Al}_2\text{O}_3$  parts with different shapes fabricated by adding small amounts of graphite were about 67.8 mm [24], as shown in Fig. 3(a), but these structures are damaged at the microscopic level. In addition, direct printing of high geometric accuracy parts is usually at the expense of densification. Similar findings have been observed for pure  $\text{ZrO}_2$  parts, including turbine blade, wall, and cube [58], which was considered to have an accurate geometry compared to the computer aided design (CAD)

**Table 2.** Geometric properties of typical ceramic structures fabricated by the DLAM processes

Process	Materials	Geometric shape	Geometric dimensions <sup>#</sup>		Geometric accuracy
			Width <sup>*</sup> / mm	Height <sup>*</sup> / mm	
SLS/SLM [24]	Al <sub>2</sub> O <sub>3</sub>	Turbine, lattice, hollow, and end cap structures	~67.8	~81.3	Good accuracy with lower-density
SLS/SLM [52]	Al <sub>2</sub> O <sub>3</sub>	Thin sheet with cracks	~10	~0.5	Lower $v$ reduces shaping accuracy
SLS/SLM [25]	Al <sub>2</sub> O <sub>3</sub>	Thin-walled structure	~10	~0.5	N/A
LDED [37]	Al <sub>2</sub> O <sub>3</sub>	Gear, stepped discoidal structure, cylinder, cube	~25	~33	N/A
LDED [38]	Al <sub>2</sub> O <sub>3</sub>	Cylinder	~5	≥200	N/A
SLS/SLM [33]	Al <sub>2</sub> O <sub>3</sub> /ZrO <sub>2</sub>	Turbine, hollow structure	~41.4	~8.1	N/A
SLS/SLM [32]	Al <sub>2</sub> O <sub>3</sub> /ZrO <sub>2</sub>	Turbine, framework	~41.4	~19.4	N/A
LDED <sub>2</sub> [42]	Al <sub>2</sub> O <sub>3</sub> /ZrO	Arc wall, cylinder	~19	~52	N/A
LDED [53]	Al <sub>2</sub> O <sub>3</sub> /ZrO <sub>2</sub>	Cylinder	~5	~230	N/A
SLS/SLM [54]	SiC	Turbine Lattice structure	~20 ~20	~20 ~25	N/A
SLS/SLM [55]	ZrO <sub>2</sub>	Turbine	~30	N/A	Relatively good accuracy
SLS/SLM [26]	ZrO <sub>2</sub>	Rectangular sheet	~25	~3–3.75	Fulfils the CAD design basically
LDED [56]	Al <sub>2</sub> O <sub>3</sub> /Al <sub>2</sub> TiO <sub>5</sub>	Cylinder Thin-walled rings	~5 ~15	~200 ~20	N/A
SLS/SLM [57]	Al <sub>2</sub> O <sub>3</sub> /GdAlO <sub>3</sub> /ZrO <sub>2</sub>	Triangular prism, hexagonal prisms, cylinders, cubic	~30	~1	Good accuracy
LDED [49]	Al <sub>2</sub> O <sub>3</sub> /GdAlO <sub>3</sub> /ZrO <sub>2</sub>	Cylinder Corner shape	~5 ~8	~410 ~64	N/A

Note: Geometric dimensions<sup>#</sup> mean the achievable maximum section widths and building heights; Width<sup>\*</sup>—Transverse section dimension; Height<sup>\*</sup>—Longitudinal section dimension; N/A—Not available.

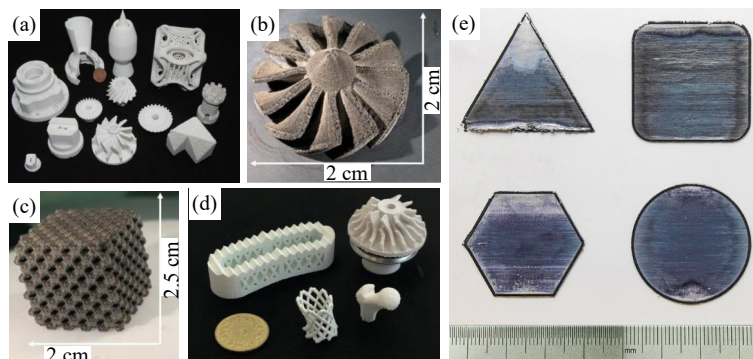


**Fig. 3.** Typical ceramic parts fabricated by SLS/SLM processes: (a) Al<sub>2</sub>O<sub>3</sub> ceramics [24]; (b, c) SiC ceramics [54]; (d) Al<sub>2</sub>O<sub>3</sub>/ZrO<sub>2</sub> ceramics [33]; (e) Al<sub>2</sub>O<sub>3</sub>/GdAlO<sub>3</sub>/ZrO<sub>2</sub> eutectic ceramics [57]. (a) Reprinted by permission from Springer Nature: *J. Mater. Res., Shaping of ceramic parts by selective laser melting of powder bed*, E. Juste, F. Petit, V. Lardot, and F. Cambier, Copyright 2014. (b, c) Reprinted from [54]. (d) Reprinted from *Addit. Manuf.*, 31, F. Verga, M. Borlaf, L. Conti, et al., Laser-based powder bed fusion of alumina toughened zirconia, 100959, Copyright 2020, with permission from Elsevier. (e) Reprinted from *Addit. Manuf.*, 72, Z.L. Shen, H.J. Su, M.H. Yu, et al., Large-size complex-structure ternary eutectic ceramic fabricated using laser powder bed fusion assisted with finite element analysis, 103627, Copyright 2020, with permission from Elsevier.

design [59], but only 56% density. Numerical simulation-guided process optimization enables the manufacturing of SiC parts with a width of 20 mm [54] (Fig. 3(b) and (c)). Regranulation appears to be a viable approach for fabricating large-size and complex-shape parts, such as SLS/SLM Al<sub>2</sub>O<sub>3</sub>/ZrO<sub>2</sub> ceramics with a width of about 41 mm and poor surface roughness [33] (Fig. 3(d)). In contrast, due to the thermal stresses, the SLS/SLM processes with fully melting features require high-temperature preheating to produce fully structured parts. Typical representatives are Al<sub>2</sub>O<sub>3</sub>/ZrO<sub>2</sub> ceramics with a width of about 41.4 mm [32], such as frameworks for dental restoration and turbines for turbochargers.

The SLM Al<sub>2</sub>O<sub>3</sub>/GdAlO<sub>3</sub>/ZrO<sub>2</sub> ternary eutectic ceramics with different shapes aided by finite element analysis (FEA) shows a width of 30 mm [57] (Fig. 3(e)). The results also show that ceramic structures with curved or rounded edges have a higher crack formation tolerance and the part is considered to have good geometric accuracy.

The LDED Al<sub>2</sub>O<sub>3</sub> gear and cylinder [37], as listed in Table 2, have a width of about 25 mm, as shown in Fig. 4(a). Al<sub>2</sub>O<sub>3</sub>/ZrO<sub>2</sub> eutectic ceramics formed by ZrO<sub>2</sub> doping with arc wall and cylinder shapes have a width of about 19 mm [42] (Fig. 4(b)). When the width is narrow (less than 6 mm), crack-free structures can be freely fabricated in the build dir-

ection (or deposition direction, Z-axis), mainly limited by the machine threshold (Fig. 4(c) and (d)) [53,56]. This argument is supported by the investigations of Su *et al.* [49], which show a height dimension of about 410 mm, as shown in Fig. 4(e). Corner-shaped structures with a width of about 8 mm can be built by adjusting the scanning strategy after process optimization, considered to have a good geometric accuracy (Fig. 4(f)). Therefore, the dimension in the build direction of LDED crack-free ceramics appears to be unrestricted, but the dimension in the vertical build direction is significantly limited due to tensile stress. An investigation of  $\text{Al}_2\text{O}_3$  ceramics demonstrated the critical effect of process parameters on the geometric properties of LDED parts [60]. This study believes that an increase in  $P$  has a positive effect on the length of the printed single track, with a slight change in width. The rise in  $v$  deteriorates the dimension accuracy,

associated with less powder entering the melt pool. However, considering the design size ( $\phi 4$  mm), the geometric accuracy of LDED mullite cylinders may be poor ( $\phi 5$ – $6$  mm) [61]. Further analysis suggests that this may be related to poor-quality deposition layers due to the high viscosity of the rapidly cooled silica-containing melt pool. Numerical simulation of the melt flow during DLAM of ceramics may be helpful. In addition, the shrinkage of DLAM ceramics is usually low due to the highly dense molding characteristics of complete solidification and melting, but reasonable control of the melt pool shape is difficult because of the extremely high temperatures. Therefore, the geometric dimensions and accuracy of DLAM ceramics need to be improved compared to other ceramic AM techniques, such as vat photopolymerization [16], digital light processing [17], and direct ink writing [62].

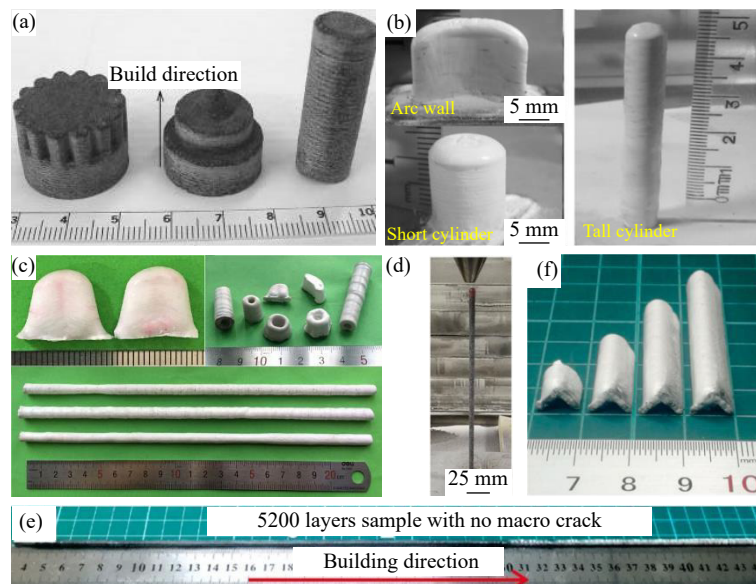


**Fig. 4.** Typical ceramic parts fabricated by LDED processes: (a)  $\text{Al}_2\text{O}_3$  ceramics [37]; (b)  $\text{Al}_2\text{O}_3/\text{ZrO}_2$  eutectic ceramics [42]; (c)  $\text{Al}_2\text{O}_3/\text{ZrO}_2$  ceramics [53]; (d)  $\text{Al}_2\text{O}_3/\text{Al}_2\text{TiO}_5$  ceramics [56]; (e, f)  $\text{Al}_2\text{O}_3/\text{GdAlO}_3/\text{ZrO}_2$  eutectic ceramics [49]. (a) V.K. Balla, S. Bose, and A. Bandyopadhyay, *Int. J. Appl. Ceram. Technol.*, 5, 234–242 (2008) [37]. Copyright John Wiley and Sons. Reproduced with permission. (b) Reprinted from *Scripta Mater.*, 95, F.Y. Niu, D.J. Wu, G.Y. Ma, J.T. Wang, M.H. Guo, and B. Zhang, Nanosized microstructure of  $\text{Al}_2\text{O}_3$ – $\text{ZrO}_2$  ( $\text{Y}_2\text{O}_3$ ) eutectics fabricated by laser engineered net shaping, 39–41, Copyright 2014, with permission from Elsevier. (c) D.J. Wu, J.D. San, F.Y. Niu, *et al.*, *Int. J. Appl. Ceram. Technol.*, 17, 227–238 (2020) [53]. Copyright John Wiley and Sons. Reproduced with permission. (d) Reprinted from *Addit. Manuf.*, 35, Y.F. Huang, D.J. Wu, D.K. Zhao, *et al.*, Process optimization of melt growth alumina/aluminum titanate composites directed energy deposition: Effects of scanning speed, 101210, Copyright 2020, with permission from Elsevier. (e, f) Reprinted from *Addit. Manuf.*, 70, H.J. Su, H.F. Liu, H. Jiang, *et al.*, One-step preparation of melt-grown  $\text{Al}_2\text{O}_3/\text{GdAlO}_3/\text{ZrO}_2$  eutectic ceramics with large size and irregular shape by directed energy deposition, 103563, Copyright 2023, with permission from Elsevier.

### 3.2. Surface roughness

Surface roughness ( $R_a$ ) is a critical parameter for evaluating part quality, referring to the degree of unevenness in the micro peaks and valleys on the part surface. Table 3 presents an investigation of  $R_a$  for DLAM ceramics [57,60,63–68]. The  $R_a$  of SLS/SLM  $\text{SiO}_2$  and  $\text{ZrSiO}_4$  ceramics increases with increasing  $P$  and decreases with increasing  $v$ , as concluded by Tang *et al.* [63]. This pattern of change was also found in the investigation of  $\text{Al}_2\text{O}_3$  parts, where Fayed *et al.* [64] concluded that the increase in laser energy density ( $Q = P/v$  or  $P/(vm)$ ) leads to the formation of larger-sized spherical struc-

tures, increasing  $R_a$ . On the other hand, an increase in  $v$  reduces the possibility of plasma formation, which decreases the  $R_a$ . Hagedorn *et al.* [65] believes that reducing the particle size in the powder bed can further improve the  $R_a$  of  $\text{Al}_2\text{O}_3/\text{ZrO}_2$  parts. Furthermore, the influence law of  $v$  on  $R_a$  was also observed by Shen *et al.* [57]. The scanning strategy is also considered one factor affecting the  $R_a$  of DLAM ceramics, and the linear-45° strategy had the lowest  $R_a$  of 97  $\mu\text{m}$  [66]. Optimizing the defocusing distances is another strategy to modulate the  $R_a$  of SLS/SLM ceramics. Xiong *et al.* [67] argues that with the increase of defocusing dis-

**Table 3.** Studies on surface roughness in DLAM-processed ceramics

Process	Main features
SLS/SLM [63]	Increase $P$ , $R_a$ increases from 21.8 to 30 $\mu\text{m}$ . Increase $v$ , $R_a$ decreases from 34.1 to 18.7 $\mu\text{m}$ .
SLS/SLM [64]	Increasing $P$ and/or decreasing $v$ leads to an increase in $R_a$ , ranging from 0.5 to 2.7 $\mu\text{m}$ .
SLS/SLM [66]	Scanning strategy significantly affects $R_a$ . Linear-45° pattern shows a low $R_a$ of 97 $\mu\text{m}$ , and island-concentric shows a high $R_a$ of 206 $\mu\text{m}$ .
SLS/SLM [65]	Preheated DLAM deteriorates the $R_a$ (150 $\mu\text{m}$ ), and decreasing powder particles improves the $R_a$ .
SLS/SLM [57]	$R_a$ can be reduced by increasing the $v$ (from 7.332 to 3.377 $\mu\text{m}$ ).
SLS/SLM [67]	$R_a$ decreases first and then increases (from 9.2 to 6.05 $\mu\text{m}$ , and then from 6.05 to 9.5 $\mu\text{m}$ ) when the defocusing distance increases from -3 to 3 mm.
LDED [60]	Increase $P$ and powder feed rate, $R_a$ decreases from 9.1 to 6.4 $\mu\text{m}$ and from 7.4 to 5.3 $\mu\text{m}$ , respectively. Increase $v$ , $R_a$ increases from 4.6 to 7.3 $\mu\text{m}$ ; further increasing $v$ , $R_a$ decreases slightly.
LDED [68]	$R_a$ increases from 0.13–0.18 to 0.65 $\mu\text{m}$ with increasing annealing temperature.
LDED [69]	Low $P$ ( $\leq 275$ W), unformed surface and high $R_a$ ; high $P$ (300 W), $R_a$ smooth surface and low $R_a$ .

tance, the  $R_a$  follows a pattern of first decreasing and then increasing. Moreover, other factors that affect the  $R_a$  of the part are adhesion of unmelted particles and wettability. As for LDED ceramics, Li *et al.* [60] conducted a detailed investigation of the  $R_a$  about LDED  $\text{Al}_2\text{O}_3$  block parts. The results indicate that the  $R_a$  gradually decreases with the increase of  $P$  and powder feed rate ( $m$ ), and first decreases and then increases with the rise of  $v$ , which may be related to the energy input to the melt pool and the degree of powder melting. For LDED  $\text{Al}_2\text{O}_3$  ceramics, Mishra *et al.* [69] concluded that as the  $P$  is increased from 225 to 300 W, the surface morphology of a single track will gradually evolve from unformed (low  $P$ ) to smooth (high  $P$ ), that is, the  $R_a$  gradually decreases. Also, laser remelting is another method to improve the  $R_a$  of DLAM ceramics [33].

### 3.3. Defects

Defects play a critical role in determining the mechanical properties and performance of DLAM ceramics. This section provides an overview of defect characterization and inhibition methods for ceramics fabricated through DLAM processes. Detailed information is summarized in Table 4 [5,24,26–27,31–33,37–40,47,56–57,61,69–74].

#### 3.3.1. Cracks

Cracking is the primary challenge in DLAM ceramics due to strong crack sensitivity. Crack formation is generally considered to be caused by the shrinkage, thermal shock, and/or thermal stress in the parts during sintering or melting [24]. The morphology of poorly dense parts with cracks and deeper cracks in SLS/SLM ceramics is shown in Fig. 5 (a)–(b). Morphologically, several studies have concluded that cracks in DLAM ceramics can be categorized into two types: longitudinal cracks and transverse cracks (Fig. 5(c)–(e)) [34,57,75]. The longitudinal cracks that usually form are more severe than the transverse cracks. Consequently, the influence of longitudinal cracks on quality is more significant. A combination of powder bed conditions, internal pores, and thermal stresses may be responsible for the formation and propagation of the two types cracks [76]. Inappropriate selection of powder bed density will lead to the formation of defects between the melt tracks due to insufficient melt, in-

creasing the susceptibility to transverse crack formation [52]. Correspondingly, the origin of longitudinal cracks may be related to the vaporization hole generated at the beginning of printing [75]. Alternatively, the non-uniform distribution of laser energy leading to the non-uniform thermal stresses may also be a reason for forming these ordered longitudinal cracks.

LDED ceramics seem more prone to cracking than SLS/SLM due to higher thermal stresses. Similar crack morphologies, longitudinal and transverse cracks, have also been found in LDED ceramics, as reported by Niu *et al.* [77]. In their case, the surface cracking of thin-walled structures in the printed state was relatively severe, and similar findings were found in printing  $\text{Al}_2\text{O}_3/\text{ZrO}_2$  ceramics (Fig. 6(a)) [53] and magnesium aluminate spinel [40]. For longitudinal cracks parallel to the build direction, cracking research for  $\text{Al}_2\text{O}_3$  ceramics [37] suggested that thermal stresses and strain discontinuities between adjoining deposited layers were responsible for forming intergranular longitudinal cracks. However, due to the complex thermal history and the built structure, thermal stress between adjacent layers does not seem to explain the formation of longitudinal cracks [66] thoroughly. For example, LDED mullite has shown that longitudinal cracks can be caused by air pores at the sample bottom and shrinkage cavities at the sample top [41], also found by Su *et al.* [49], as shown in Fig. 6(b). Consequently, cracking of DLAM ceramics from the bottom seems to be a high probability occurrence, resulting in longitudinal cracks with secondary for transverse cracks in severe circumstances (Fig. 6(c)). Therefore, numerical simulation combined with the thermal performance of ceramics for the detailed heat and stress distribution of the DLAM processes is necessary to clarify the crack initiation mechanism and propose practical inhibition approaches.

#### 3.3.2. Voids

Void is another critical factor affecting the property and performance of DLAM ceramics. However, avoiding void formation is challenging, especially for deposition of ceramics [78]. There are several types of voids, such as poorly bonded voids, lack of fusion, and air pores, as shown in Fig. 7. Poorly bonded voids are common in SLS/SLM parts and result from the solid sintering or partial melting (Fig. 7(a)) [59].

**Table 4.** Defect characteristics and relative density of ceramics fabricated by the DLAM processes

Material	Processes	Relative density / %	Defect characteristics and formation mechanism	Process parameters for low-defect parts
Al <sub>2</sub> O <sub>3</sub> [70]	SLS/SLM	85	Cracks: stop at the solidified surface end, resulting from thermal deformation (curling). Voids: distributed between microstructures, caused by incomplete melting.	$P = 2 \text{ W}$ , $v = 5.2 \text{ mm/s}$
Al <sub>2</sub> O <sub>3</sub> [24]	SLS/SLM	>90	Cracks: thermal shocks and/or thermal stresses induced by a heterogeneous sintering. Voids: a consequence of stacking defects in the powder bed.	$Q = 16.6 \text{ J/mm}^2$
Al <sub>2</sub> O <sub>3</sub> [37]	LDED	94	Cracks: crack-free, cracking caused by thermal stresses when the process is not appropriate. Voids: low energy densities for highly porous ceramics caused by incomplete melting.	$P = 175 \text{ W}$ , $v = 10 \text{ mm/s}$
Al <sub>2</sub> O <sub>3</sub> [38]	LDED	99.5	Cracks: crack-free. Voids: small spherical pores, formed by decreased solubility of gases; large ellipsoidal pores are formed by agglomeration of small pores.	$P = 375 \text{ W}$ , $v = 300 \text{ mm/min}$
Al <sub>2</sub> O <sub>3</sub> [69]	LDED	≤95	Cracks: appeared after printing of six layers. Voids: distributed at different locations on the part.	$P = 300 \text{ W}$ , $v = 0.6 \text{ mm/min}$
ZrO <sub>2</sub> [71]	SLS/SLM	84–91	Cracks: vertical ordered crack and crossing crack. Voids: small pores evolve into large pores, which rupture to form cracks.	Preheating above 1500°C
ZrO <sub>2</sub> [26]	SLS/SLM	96.5	Cracks and voids: cracks are present between the columns and the pores are 1 μm.	$P = 84 \text{ W}$ , $v = 70 \text{ mm/s}$
ZrO <sub>2</sub> [39]	LDED	98.7	Crack: vertical and horizontal cracks.	$P = 325 \text{ W}$ , $v = 355 \text{ mm/min}$
SiC [27]	SLS/SLM	87	Voids: high porosity, powders not fully melting. Layer degradation and decomposition.	$P = 45 \text{ W}$ , $v = 100 \text{ mm/s}$
High-entropy carbide [31]	SLS/SLM	>99	Cracks: free-crack. Voids: free-pore.	$P = 300\text{--}600 \text{ W}$ , $v = 0.22 \text{ mm/s}$
MgAl <sub>2</sub> O <sub>4</sub> [40]	LDED	98	Crack length and pores increase with increasing $P$ .	$P = 275 \text{ W}$ , $v = 0.7 \text{ mm/min}$
Mullite [61]	LDED	97.8	Cracks: distributed in the sample center. Voids: large pores are distributed at the sample edge.	$P = 300 \text{ W}$ , $v = 200 \text{ mm/min}$
Al <sub>2</sub> O <sub>3</sub> /ZrO <sub>2</sub> [32]	SLS/SLM	~100	Cracks: small parallel cracks.	Preheat the powder bed to 1600°C
Al <sub>2</sub> O <sub>3</sub> /ZrO <sub>2</sub> [33]	SLS/SLM	96	Cracks: cracks smaller than 1 μm in thickness and several micrometers in length.	N <sub>2</sub> shielding atmosphere
Al <sub>2</sub> O <sub>3</sub> /ZrO <sub>2</sub> [72]	LDED	98.3	Cracks and cavities are distributed in the cellular structure boundaries.	$P = 530 \text{ W}$ , $v = 400 \text{ mm/min}$
Al <sub>2</sub> O <sub>3</sub> /ZrO <sub>2</sub> [73]	LDED	N/A	Crack: longitudinal crack in the bottom center, transverse crack in the middle edge. Voids: spherical air pore and irregular shrinkage cavity.	Ultrasound-assisted, 120 W
Al <sub>2</sub> O <sub>3</sub> /ZrO <sub>2</sub> [47]	LDED	~97	Crack: expand in both transverse and longitudinal directions. Voids: porosity increases with increasing ZrO <sub>2</sub> content.	Add 10wt% ZrO <sub>2</sub>
Al <sub>2</sub> O <sub>3</sub> /Al <sub>2</sub> TiO <sub>5</sub> [56]	LDED	98	Cracks: several branched longitudinal dendritic cracks at low $v$ . Voids: small pores are distributed inside the sample.	Rapid scanning, 900 mm/min
Al <sub>2</sub> O <sub>3</sub> /mullite [5]	LDED	≤99.4	Cracks: multiple transverse cracks and some longitudinal cracks. Voids: small pore morphology distributed inside samples with low Al <sub>2</sub> O <sub>3</sub> content.	$P = 275 \text{ W}$ , $v = 0.7 \text{ mm/min}$
Al <sub>2</sub> O <sub>3</sub> /GdAlO <sub>3</sub> /ZrO <sub>2</sub> [57]	SLS/SLM	N/A	Cracks: transverse and longitudinal cracks, formed by tensile and shearing stress. Voids: small-size pores at the track center, and large-size pores at the track edge.	$P = 300 \text{ W}$ , $v = 300 \text{ mm/s}$ Finite element analysis
Al <sub>2</sub> O <sub>3</sub> /GdAlO <sub>3</sub> /ZrO <sub>2</sub> [74]	LDED	98.7	Cracks: large cracks form when deposited layers increase to 100.	Preheating substrate, shortening scan length, and laser remelting

Insufficient laser intensity, uneven laser energy distribution, or inappropriate processing parameters in the SLS/SLM and LDED processes can lead to inadequate liquid phase into the solidified layer, forming a lack fusion (**Fig. 7(b)**). The shrinkage band distributed on top of LDED parts is a type of lack of fusion formed by merging a series of shrinkage cavities (**Fig. 6(c)**). Shrinkage cavities are usually created by the failure of

the liquid to fill the gap because of the rapid solidification at the top part, which can be removed by further laser remelting. Air pores are prevalent in DLAM ceramics, as shown in **Fig. 7(c)**. Specifically, bubble nuclei, due to the low solubility of gases, float, merge, and grow under driving forces (e.g., buoyancy and surface tension), failing to escape from the rapidly solidifying melt pool and forming air pores. Further-

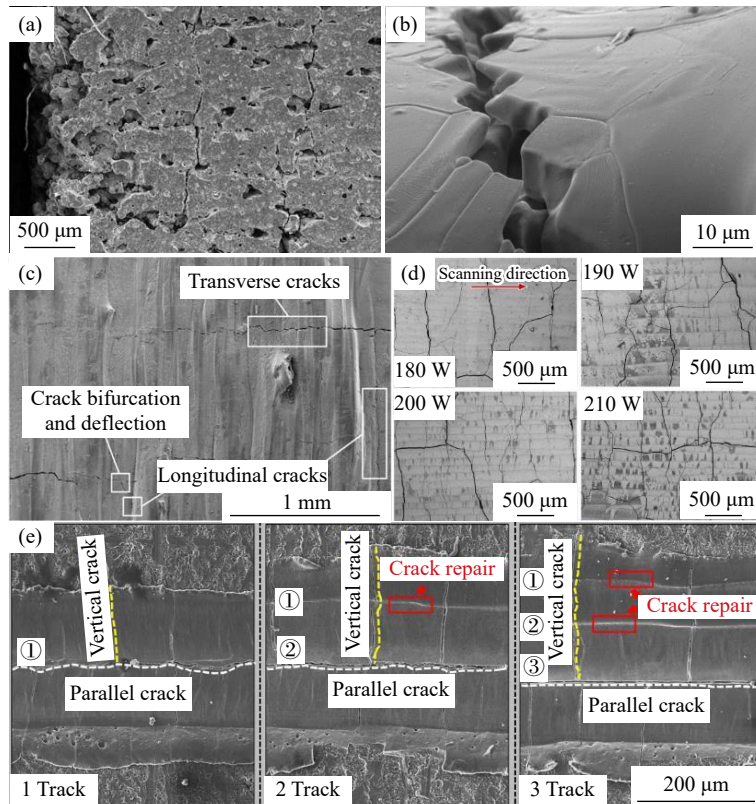


**Fig. 5. Cracking characteristics of the SLS/SLM-processed ceramics:**  $\text{Al}_2\text{O}_3$  ceramics made by (a) spray-dried  $\text{Al}_2\text{O}_3$  powder [24], (b) a slurry with  $\text{Al}_2\text{O}_3$  powder, disinfectol, and  $\text{HNO}_3$  [70], and (c) CT3000 SG grade  $\text{Al}_2\text{O}_3$  powder with an irregular sheet structure [75]; (d)  $\text{Al}_2\text{O}_3/\text{GdAlO}_3/\text{ZrO}_2$  eutectic ceramics under different laser powers [57]; (e)  $\text{Al}_2\text{O}_3/\text{ZrO}_2$  eutectic ceramics in different tracks [34]. (a) Reprinted by permission from Springer Nature: *J. Mater. Res.*, Shaping of ceramic parts by selective laser melting of powder bed, E. Juste, F. Petit, V. Lardot, and F. Cambier, Copyright 2014. (b) Reprinted from *Phys. Procedia*, 56, J. Deckers, S. Meyers, J.P. Kruth, and J. Vleugels, Direct selective laser sintering/melting of high density alumina powder layers at elevated temperatures, 117–124, Copyright 2014, with permission from Elsevier. (c) Reprinted from *Ceram. Int.*, 45, Y. Zheng, K. Zhang, T.T. Liu, W.H. Liao, C.D. Zhang, and H. Shao, Cracks of alumina ceramics by selective laser melting, 175–183, Copyright 2019, with permission from Elsevier. (d) Reprinted from *Addit. Manuf.*, 72, Z.L. Shen, H.J. Su, M.H. Yu, et al., Large-size complex-structure ternary eutectic ceramic fabricated using laser powder bed fusion assisted with finite element analysis, art. No. 103627, Copyright 2020, with permission from Elsevier. (e) Y. Zhang, K. Zhang, D. Chen, et al., *J. Am. Ceram. Soc.*, 107, 2128–2142 (2024) [34]. Copyright John Wiley and Sons. Reproduced with permission.

more, the primary gas sources are surface entrainment, internal carryover of powders, and evaporation of low melting point substances [45]. The complete voids morphology and distribution inside DLAM ceramics can be obtained by the synchrotron-based X-ray micro-computed tomography (SR- $\mu$ CT) (shown in Fig. 7(d) and (e)) [69] and deep-learning-based porosity analysis method [79], which give exciting fabrication and post-processing methods to scrutinize the voids formation and distribution of deposited ceramics. As a result, LDED parts have lower voids than SLS/SLM with solid sintering or partial melting, with densities above 95%, due to the full melting bond mechanism.

### 3.3.3. Inhibition approaches

Many approaches have been investigated to fabricate dense and crack-free ceramics, including process optimization, preheating powder bed or substrate, ultrasound-assistance, adding enhancement phases, and laser remelting as listed in Table 4. Process optimization was a preferred and easy method to inhibit defects. However, the SLS ceramic parts with complex-shape were insufficiently dense [58] and al-

ways needed to be post-treated, e.g., by hot isostatic pressing (HIP). Process optimization alone is laborious, although promising for single-step fabricating ceramics by SLM and LDED processes. The process window for high-quality LDED ceramics was narrow due to higher thermal stress and crack susceptibility [77]. In addition, the voids and cracking of LDED  $\text{Al}_2\text{O}_3$  parts were significantly reduced when the substrate material was changed from  $\text{Al}_2\text{O}_3$  to Ti–6Al–4V alloy [69]. Preheating powder bed or substrate for DLAM effectively decreases thermal stress to reduce cracking. The main energy sources for preheating are laser beams [71], induction heating (Fig. 8(a)) [80], and microwaves [81]. However, the poor surface quality of preheated parts is a tricky issue [82], such as the significant increase in  $R_a$  of SLM ceramics. The cost and safety are other issues that need to be noted. For an ultrasound-assisted deposition condition, mechanical, cavitation, and acoustic flow effects created by ultrasonic vibrations can promote rapid fluid flow on both sides of the melt pool, significantly reducing porosity and decreasing the possibility of cracking [45], as shown in Fig.

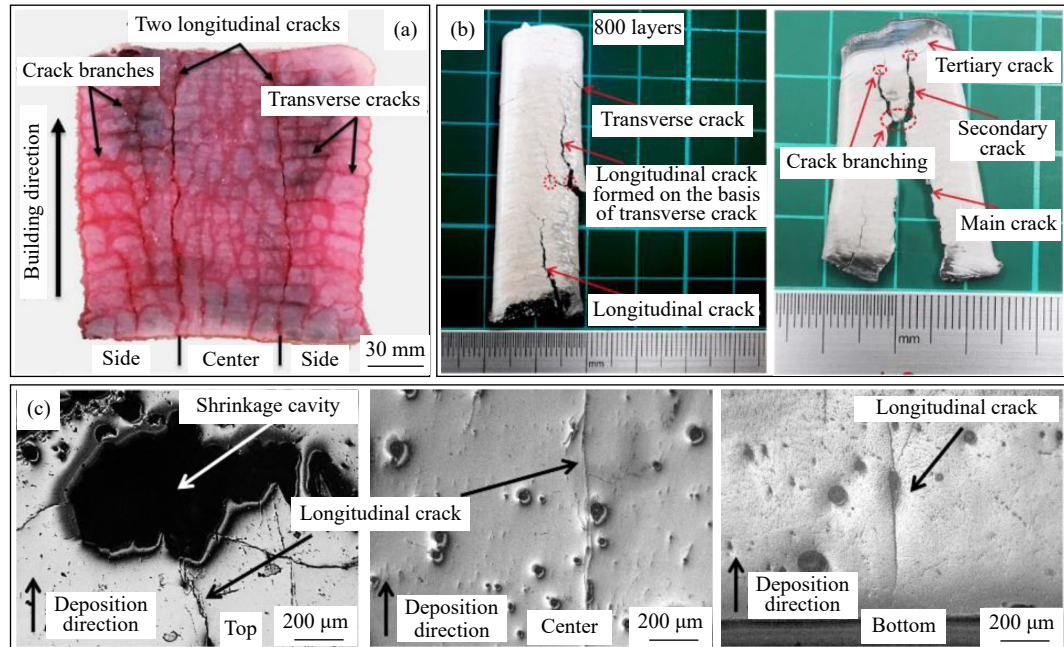


**Fig. 6.** Characteristics of cracks in LDED-processed ceramics: (a)  $\text{Al}_2\text{O}_3/\text{ZrO}_2$  ceramics [53]; (b)  $\text{Al}_2\text{O}_3/\text{GdAlO}_3/\text{ZrO}_2$  eutectic ceramics with different crack bifurcations [49]; (c) mullite under different locations [41]. (a) D.J. Wu, J.D. San, F.Y. Niu, et al., *Int. J. Appl. Ceram. Technol.*, vol. 17, 227–238 (2020) [53]. Copyright John Wiley and Sons. Reproduced with permission. (b) Reprinted from *Addit. Manuf.*, 70, H.J. Su, H.F. Liu, H. Jiang, et al., One-step preparation of melt-grown  $\text{Al}_2\text{O}_3/\text{GdAlO}_3/\text{ZrO}_2$  eutectic ceramics with large size and irregular shape by directed energy deposition, 103563, Copyright 2023, with permission from Elsevier. (c) Reprinted from *J. Alloys Compd.*, 871, D.J. Wu, D.K. Zhao, Y.F. Huang, F.Y. Niu, and G.Y. Ma, Shaping quality, microstructure, and mechanical properties of melt-grown mullite ceramics by directed laser deposition, 159609, Copyright 2021, with permission from Elsevier.

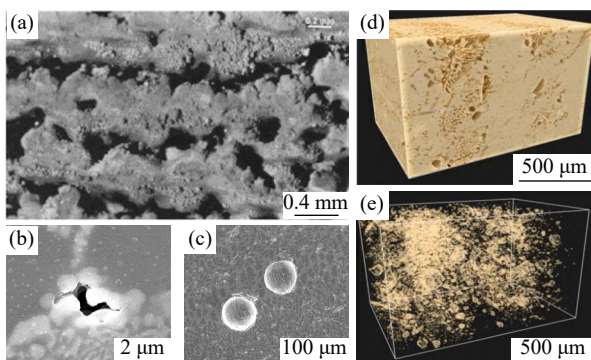


**Fig. 7.** Characteristics of voids in DLAM-processed ceramics: (a) poorly bonded voids [59]; (b) lack of fusion [45]; (c) air pores [45]; (d, e) void characteristics obtained by micro-computed tomography ((d) solid mass distribution and (e) corresponding porosity distribution) [69]. (a) Reprinted from *Appl. Surf. Sci.*, 254, I. Shishkovsky, I. Yadroitsev, P. Bertrand, and I. Smurov, Alumina-zirconium ceramics synthesis by selective laser sintering/melting, 966–970, Copyright 2007, with permission from Elsevier. (b, c) Reprinted from *Addit. Manuf.*, 28, S. Yan, Y.F. Huang, D.K. Zhao, F.Y. Niu, G.Y. Ma, and D.J. Wu, 3D printing of nano-scale  $\text{Al}_2\text{O}_3\text{-ZrO}_2$  eutectic ceramic: Principle analysis and process optimization of pores, 120–126, Copyright 2019, with permission from Elsevier. (d, e) Reprinted from *Ceram. Int.*, 47, G.K. Mishra, C.P. Paul, A.K. Rai, A.K. Agrawal, S.K. Rai, and K.S. Bindra, Experimental investigation on laser directed energy deposition based additive manufacturing of  $\text{Al}_2\text{O}_3$  bulk structures, 5708–5720, Copyright 2021, with permission from Elsevier.

8(b). The addition of enhancement phases to fabricate DLAM composite ceramics creates a variety of toughening mechanisms, and increasing the energy required for crack formation and propagation can also inhibit defect formation. Mechanical agitation of the hard particles or fiber during the DLAM process also provides the potential for bubble breakage and escape. These reinforcing phases are mainly SiC [83] and C fiber [84]. Furthermore, the optimization of laser remelting [74] and scanning strategy [69] are other effective approaches to suppress defects in DLAM ceramics. This is because these approaches modulate the thermal history and the mass-energy transport in the melt pool. In addition, the morphology of the high temperature melt pool is affected by both thermal and mass histories, insufficient temperature results in unmelted and adherent powders, increasing porosity, while high temperature gradients ( $G$ ) form higher thermal stresses, leading to cracking. Thorough flow will modulate the melt pool flow with explicit thermal history, and numerical simulation is a solution to this problem [85]. Therefore, the in-depth revelation of thermal mass flow in the melt pool is a prerequisite for further understanding the voids formation mechanism.

#### 4. Microstructures of DLAM ceramics

DLAM ceramics have a microstructure different from conventional sintering due to particular process principles and complex thermal histories, and these key features in-

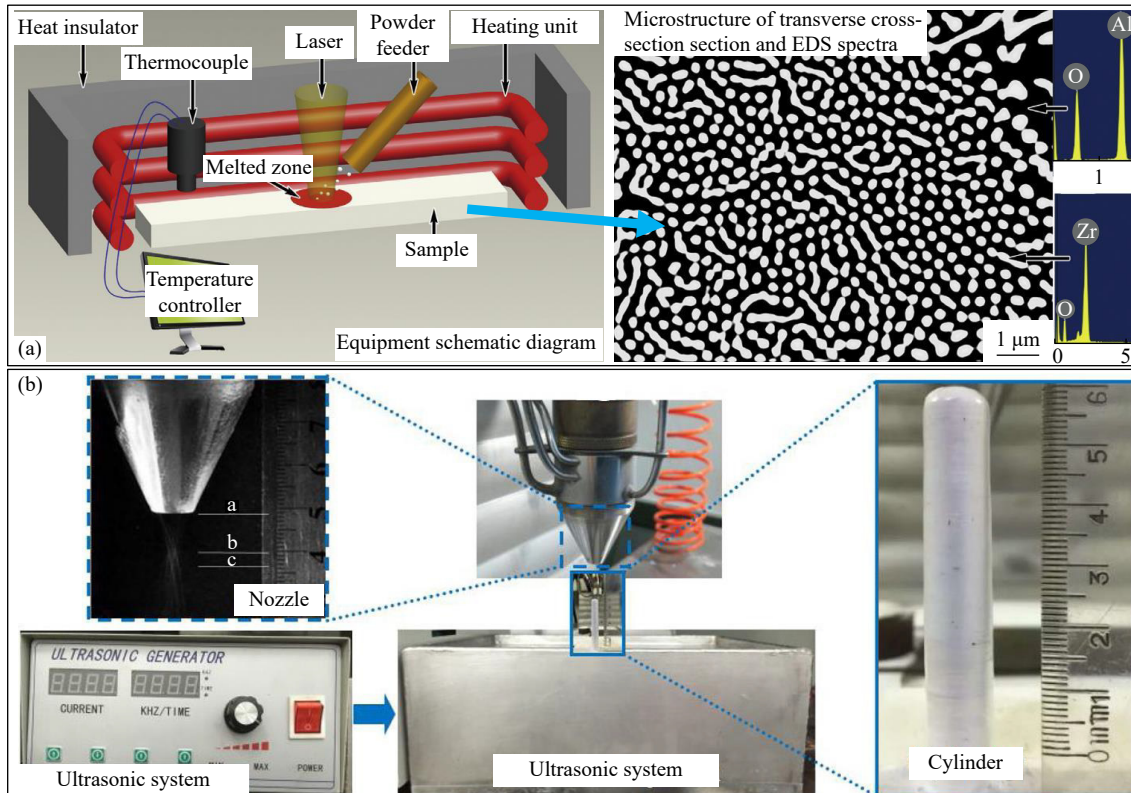


**Fig. 8.** Defect inhibition approaches in DLAM-processed ceramics: (a) preheating [80]; (b) ultrasound assistance [45]. (a) Reprinted from *J. Mater. Sci. Technol.*, 32, Z. Liu, K. Song, B. Gao, *et al.*, Microstructure and mechanical properties of  $\text{Al}_2\text{O}_3/\text{ZrO}_2$  directionally solidified eutectic ceramic prepared by laser 3D printing, 320–325, Copyright 2016, with permission from Elsevier. (b) Reprinted from *Addit. Manuf.*, 28, S. Yan, Y.F. Huang, D.K. Zhao, F.Y. Niu, G.Y. Ma, and D.J. Wu, 3D printing of nano-scale  $\text{Al}_2\text{O}_3\text{-ZrO}_2$  eutectic ceramic: Principle analysis and process optimization of pores, 120–126, Copyright 2019, with permission from Elsevier.

fluence the part performance. This section focuses on  $\text{Al}_2\text{O}_3$  and  $\text{Al}_2\text{O}_3$ -based composites, interspersed with other single-phase ceramics, and discusses the microstructure of DLAM ceramics.

#### 4.1. $\text{Al}_2\text{O}_3$ ceramics

The microstructure of  $\text{Al}_2\text{O}_3$  ceramics fabricated by SLS/SLM with solid sintering or partial melting is partially dense, consisting of a near powder-like structure and consolidated  $\text{Al}_2\text{O}_3$  droplets separated by pores [70], as shown in Fig. 9(a) and (b). The spherical structure size (grain size) of the consolidated  $\text{Al}_2\text{O}_3$  can be controlled by optimizing process parameters [64]. While the microstructure of a single track  $\text{Al}_2\text{O}_3$  ceramics produced by SLS/SLM with full melting is dominated by columnar dendrites. Equiaxial dendrites are formed at the top of the single passes when the  $Q$  is increased to a certain level (Fig. 9(c)). Fully melting of  $\text{Al}_2\text{O}_3$  ceramics using laser seems difficult due to the reflection and low absorption rate of laser radiation. The microstructure can be optimized to promote anisotropic grain growth or equiaxialization by doping micro-metal oxide to increase the absorption rate and improve the powder bed density [86]. The LDED  $\text{Al}_2\text{O}_3$  grains tend to grow epitaxially in the build direction, as shown in Fig. 9(d)–(f). In contrast, the other directions are suppressed due to the strong one-dimensional heat loss of the solidification layer through the substrate, regu-

larly arranged in parallel. The textured  $\text{Al}_2\text{O}_3$  ceramics maintain a single-phase composition consistent with the initial material, which is stable  $\alpha\text{-Al}_2\text{O}_3$  [38]. Increasing the  $v$  inhibits grain growth and triggers the transition from columnar to equiaxed crystals, resulting in grain refinement. Furthermore, optimizing the scanning strategy also seems to optimize the microstructure [69], similar to the process parameters by controlling the solidification conditions (temperature gradients  $G$  and solidification rate  $R$ ), but further investigation is needed.

#### 4.2. $\text{Al}_2\text{O}_3$ -based composites

Oxide eutectic ceramics, also known as melt growth composites (MGC), prepared by directional solidification, have stirred great enthusiasm in the field of DLAM ceramics due to their excellent properties [87]. The typical microstructure of the DLAM  $\text{Al}_2\text{O}_3/\text{ZrO}_2$  eutectic ceramics is a columnar colony structure with a light  $t\text{-ZrO}_2$  phase embedded in a dark  $\alpha\text{-Al}_2\text{O}_3$  matrix, as shown in Fig. 10(a). Specifically, fine and regular lamellar  $t\text{-ZrO}_2$  are diffused in the columnar  $\text{Al}_2\text{O}_3$  colony structure [42]. These two phases are in nanoscale and the phase interface is clean and free of amorphous phases, with a eutectic spacing of about 50–100 nm (Fig. 10(b)) [45]. Moreover, in DLAM eutectic ceramics, periodic banded structures (PBSs) along the build direction are a noteworthy feature because they significantly affect mechanical properties (Fig. 10(c) and (d)) [50, 74, 88]. The thermal influence of

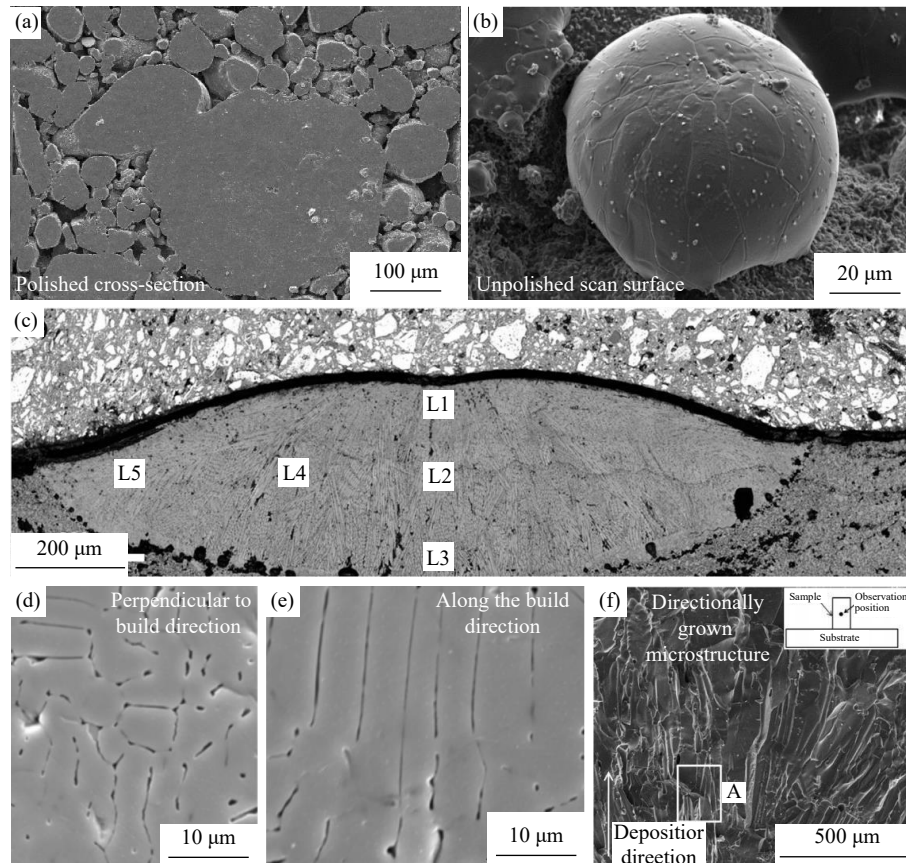


**Fig. 9.** Microstructure characteristics of  $\text{Al}_2\text{O}_3$  ceramics fabricated by DLAM processes: (a, b) SLS/SLM [70]; (c) SLM [25]; (d–f) LDED [37–38]. (a, b) Reprinted from *Phys. Procedia*, 56, J. Deckers, S. Meyers, J.P. Kruth, and J. Vleugels, Direct selective laser sintering/melting of high density alumina powder layers at elevated temperatures, 117–124, Copyright 2014, with permission from Elsevier. (c) Reprinted from *Ceram. Int.*, 44, Z.Q. Fan, M.Y. Lu, and H. Huang, Selective laser melting of alumina: A single track study, 9484–9493, Copyright 2018, with permission from Elsevier. (d, e) V.K. Balla, S. Bose, and A. Bandyopadhyay, *Int. J. Appl. Ceram. Technol.*, 5, 234–242 (2008) [37]. Copyright John Wiley and Sons. Reproduced with permission. (f) Reprinted from *Ceram. Int.*, 44, F.Y. Niu, D.J. Wu, F. Lu, G. Liu, G.Y. Ma, and Z.Y. Jia, Microstructure and macro properties of  $\text{Al}_2\text{O}_3$  ceramics prepared by laser engineered net shaping, 14303–14310, Copyright 2018, with permission from Elsevier.

the upper deposited layer, the epitaxial growth of the solidified microstructure, and the microstructural coarsening behavior (MCZs), similar to that of the heat-affected zone (HAZ) in laser welding have been applied to explain the formation of PBSs in DLAM eutectic ceramics. However, the relationship between PBSs and the deposited layers interface needs to be revealed. For example, electron backscatter diffraction (EBSD) analysis at the boundary of PBSs containing coupled zone, transition zone, and HAZ, reveals a random crystallographic orientation attributed to the initial uncoupled growth at the bottom of a melt pool [44]. This provides detailed information about the relationship between PBSs and deposited layers. In contrast, in rapid directional solidification, the formation of PBSs can be intuitively explained as periodic oscillations of the solidification interface. Therefore, the formation mechanism of PBSs found in DLAM eutectic ceramics seems to require a more detailed investigation. It is worth pointing out that the microstructure of DLAM  $\text{Al}_2\text{O}_3/\text{ZrO}_2$  composites can be optimized after adjusting material composition, showing the evolution patterns of microstructure with cellular, undeveloped dendritic, dendritic for hypoeutectic ceramics, or the opposite for hypereutectic

ceramics. In addition, 3D quasi-continuous network structures (3DQCN) have also been found in DLAM composites when  $\text{ZrO}_2$  is below the eutectic ratio, which is believed to contribute to mechanical property enhancement [43].

$\text{Al}_2\text{O}_3/\text{Y}_3\text{Al}_5\text{O}_{12}$  and  $\text{Al}_2\text{O}_3/\text{GdAlO}_3$  (GAP) eutectic are another two cases of binary eutectic ceramics fabricated by DLAM processes. The dominant microstructure of LDED  $\text{Al}_2\text{O}_3/\text{Y}_3\text{Al}_5\text{O}_{12}$  eutectic ceramics is the 3D interpenetrating network structure ('Chinese script' patterns) with fine irregular eutectic, comprising of a dark  $\text{Al}_2\text{O}_3$  phase and a bright  $\text{Y}_3\text{Al}_5\text{O}_{12}$  phase, shown in Fig. 11. The formation of irregular eutectic is related to the higher melting entropy of the two phases. In this case, the  $\text{Al}_2\text{O}_3$  grows continuously along the  $<10\bar{1}0>$  crystallographic orientation, while the  $\text{Y}_3\text{Al}_5\text{O}_{12}$  changes from random to competitive growth, which can be explained by the Magnin-Kurz model [51]. Substrate water cooling can change the microstructure from a typical network structure to a colony and dendritic structure, and the eutectic spacing will be reduced by 78.1% [89]. Correspondingly, the HAZ roughly affected the microstructure of SLS/SLM  $\text{Al}_2\text{O}_3/\text{GAP}$  eutectic ceramics between adjacent deposited layers, in which the  $\text{Al}_2\text{O}_3$  and GAP phases were

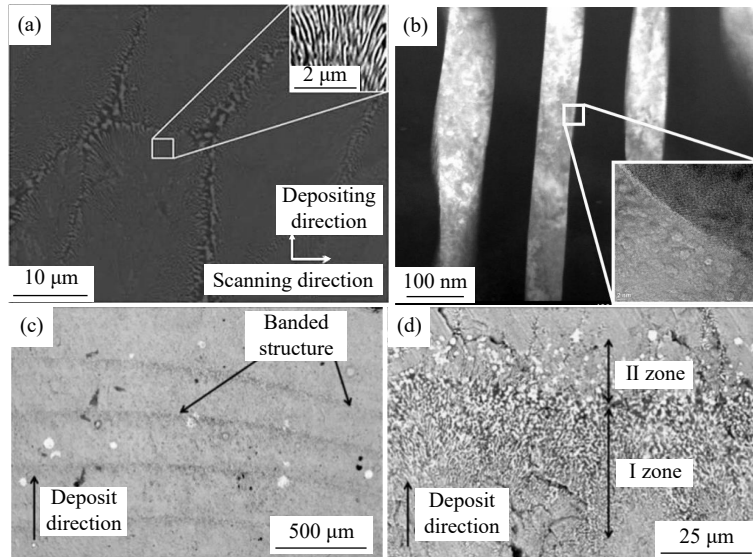


**Fig. 10.** Microstructure characteristics of  $\text{Al}_2\text{O}_3/\text{ZrO}_2$  eutectic ceramics fabricated by DLAM processes: (a) typical microstructure with a colony structure [42]; (b) microstructure with finer eutectic spacing [45]; (c, d) microstructure with periodic banded structures [88]. (a) Reprinted from *Scripta Mater.*, 95, F.Y. Niu, D.J. Wu, G.Y. Ma, J.T. Wang, M.H. Guo, and B. Zhang, Nanosized microstructure of  $\text{Al}_2\text{O}_3$ - $\text{ZrO}_2$  ( $\text{Y}_2\text{O}_3$ ) eutectics fabricated by laser engineered net shaping, 39–41, Copyright 2014, with permission from Elsevier. (b) Reprinted from *Addit. Manuf.*, 28, S. Yan, Y.F. Huang, D.K. Zhao, F.Y. Niu, G.Y. Ma, and D.J. Wu, 3D printing of nano-scale  $\text{Al}_2\text{O}_3$ - $\text{ZrO}_2$  eutectic ceramic: Principle analysis and process optimization of pores, 120–126, Copyright 2019, with permission from Elsevier. (c, d) Reprinted from *Ceram. Int.*, 43, S. Yan, D.J. Wu, G.Y. Ma, F.Y. Niu, R.K. Kang, and D.M. Guo, Formation mechanism and process optimization of nano  $\text{Al}_2\text{O}_3$ - $\text{ZrO}_2$  eutectic ceramic via laser engineered net shaping (LENS), 14742–14747, Copyright 2017, with permission from Elsevier.

uniform ‘Chinese script’ patterns [35]. The microstructure inside the deposited layers is typical of a colony structure, consisting of ‘Chinese script’ patterns, lamellar patterns, and rod-like patterns.

One of the cases for ternary eutectic ceramics fabricated by DLAM is  $\text{Al}_2\text{O}_3/\text{GdAlO}_3/\text{ZrO}_2$ . The key feature of the microstructure for SLS/SLM  $\text{Al}_2\text{O}_3/\text{GdAlO}_3/\text{ZrO}_2$  is the colony structure with a ‘Chinese script’ patterns, lamellar patterns, and rod-like patterns, internally composed of a black  $\text{Al}_2\text{O}_3$

phase, a gray  $\text{ZrO}_2$  phase, and a white  $\text{GdAlO}_3$  phase [36]. Similarly, the microstructure of LDED  $\text{Al}_2\text{O}_3/\text{GdAlO}_3/\text{ZrO}_2$  ternary eutectic ceramics also has eutectic structures such as colony structure and ‘Chinese script’ patterns, shown in Fig. 12 [90]. Moreover, another ternary eutectic ceramics fabricated by LDED is  $\text{Al}_2\text{O}_3/\text{Y}_3\text{Al}_5\text{O}_{12}/\text{ZrO}_2$  [50], with the microstructure of monocrystal cellular eutectics. The texture along the building direction is  $<0001>_{\text{Al}_2\text{O}_3} // <001>_{\text{Y}_3\text{Al}_5\text{O}_{12}} // <001>_{\text{ZrO}_2}$ , gradually inclined from the center to the edge.

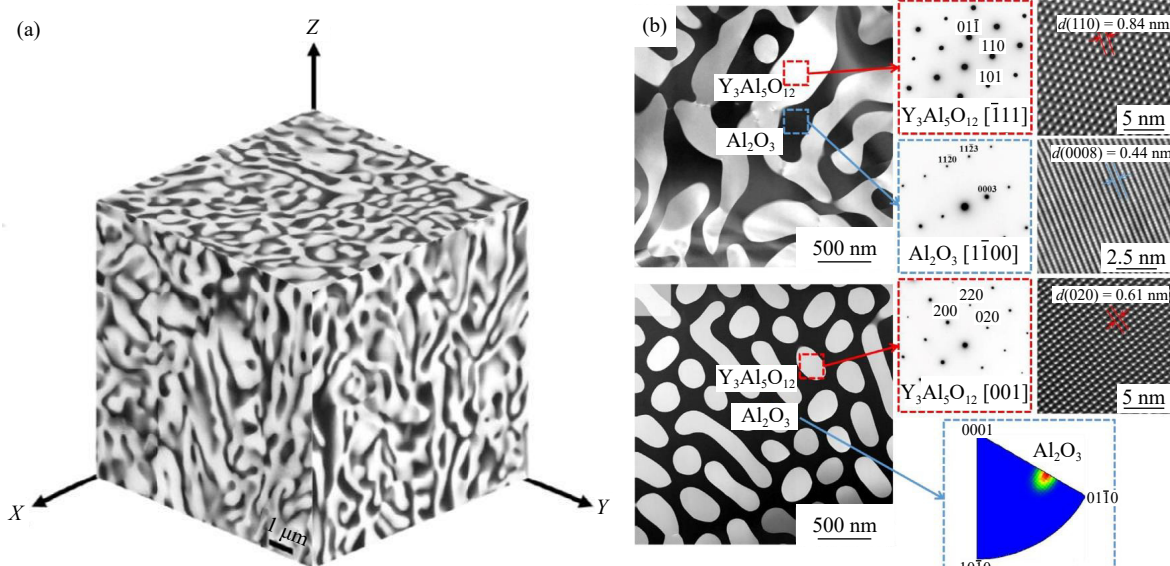


**Fig. 11.** Interfacial structures of  $\text{Al}_2\text{O}_3/\text{Y}_3\text{Al}_5\text{O}_{12}$  eutectic ceramics fabricated by LDED process [51]: (a) isometric view showing the dominant microstructure; (b) TEM analysis of typical  $\text{Al}_2\text{O}_3$ - $\text{Y}_3\text{Al}_5\text{O}_{12}$  irregular eutectics. Reprinted from *Scripta Mater.*, 178, Z.Q. Fan, Y.T. Zhao, Q.Y. Tan, B.W. Yu, M.X. Zhang, and H. Huang, New insights into the growth mechanism of 3D-printed  $\text{Al}_2\text{O}_3$ - $\text{Y}_3\text{Al}_5\text{O}_{12}$  binary eutectic composites, 274–280, Copyright 2020, with permission from Elsevier.

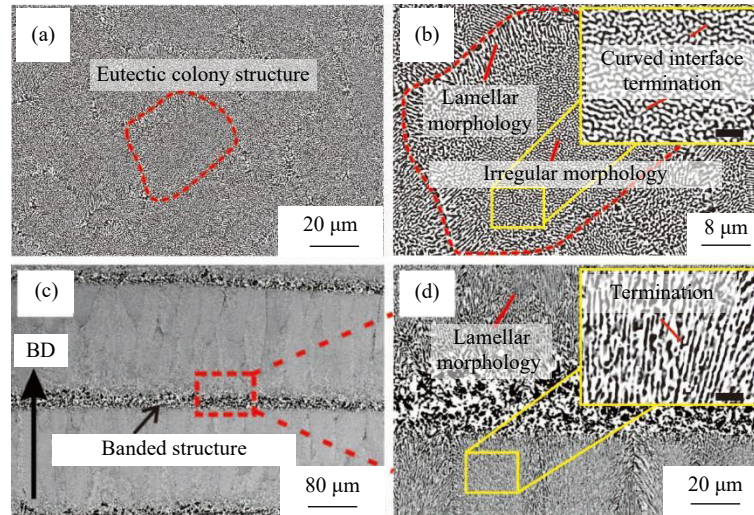


**Fig. 12.** Microstructure characteristics of  $\text{Al}_2\text{O}_3/\text{GdAlO}_3/\text{ZrO}_2$  ternary eutectic ceramics fabricated by LDED process [90]: (a) transverse microstructure; (b) magnified view of (a); (c) longitudinal microstructure; (d) magnified view of (c). Reprinted from *J. Mater. Sci. Technol.*, 85, H.F. Liu, H.J. Su, Z.L. Shen, et al., Preparation of large-size  $\text{Al}_2\text{O}_3/\text{GdAlO}_3/\text{ZrO}_2$  ternary eutectic ceramic rod by laser directed energy deposition and its microstructure homogenization mechanism, 218–223, Copyright 2020, with permission from Elsevier.

*In situ* synthesized  $\text{Al}_2\text{O}_3/\text{Al}_2\text{TiO}_5$  [91] and  $\text{Al}_2\text{O}_3$ /mullite [5] are other representatives of DLAM  $\text{Al}_2\text{O}_3$ -based composites. They usually contain *in situ* synthesized  $\text{Al}_2\text{TiO}_5$  or mullite dispersed in the continuous  $\text{Al}_2\text{O}_3$  matrix [48]. The morphology and content of the  $\text{Al}_2\text{TiO}_5$  phase or mullite phase vary with process parameters and material composition under the influence of solidification conditions ( $G$  and  $R$ ), as shown in Fig. 13. For example, with increasing  $Q$ , the microstructure of LDED  $\text{Al}_2\text{O}_3/\text{Al}_2\text{TiO}_5$  composites depos-

ited by  $\text{Al}_2\text{O}_3$  and  $\text{TiO}_2$  powders evolves from isotropic growth to anisotropic growth, which the non-equilibrium solidification theory can explain. Similarly, as the  $\text{Al}_2\text{O}_3$  content in the initial material increases, the microstructure of LDED  $\text{Al}_2\text{O}_3$ /mullite composites deposited by  $\text{Al}_2\text{O}_3$  and  $\text{SiO}_2$  powders evolves from anisotropic growth (equiaxial dendrites) to isotropic growth (columnar crystals), which can be explained by the nucleation theory and compositional supercooling theory.

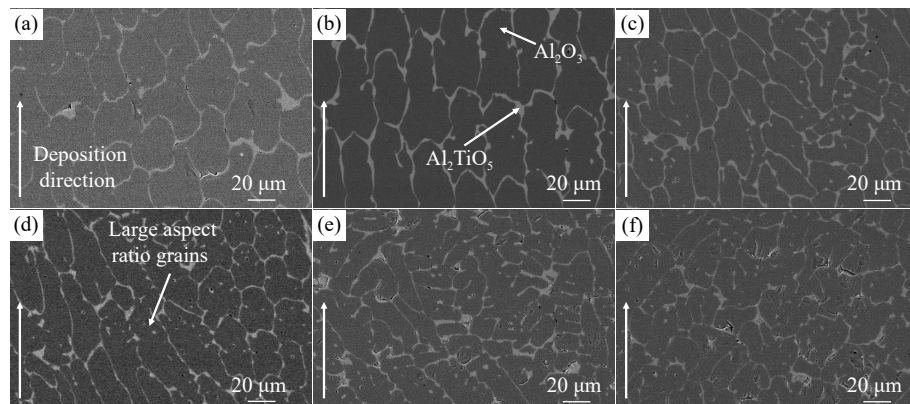


**Fig. 13.** Microstructure characteristics of  $\text{Al}_2\text{O}_3/\text{Al}_2\text{TiO}_5$  composites fabricated by LDED process with different scanning speeds [56]: (a) 50 mm/min; (b) 100 mm/min; (c) 300 mm/min; (d) 500 mm/min; (e) 700 mm/min; (f) 900 mm/min. Reprinted from *Addit. Manuf.*, 35, Y.F. Huang, D.J. Wu, D.K. Zhao, et al., Process optimization of melt growth alumina/aluminum titanate composites directed energy deposition: Effects of scanning speed, 101210, Copyright 2020, with permission from Elsevier.

#### 4.3. Other ceramics

In the case of SLS/SLM  $\text{SiO}_2$  ceramics, the sand particles were sintered together but underwent partial melting due to the low energy input. Additionally, the surfaces of particles were melted and connected through ‘bridges’ [63]. The microstructure of SLS/SLM  $\text{Y}_2\text{O}_3$  stabilized  $\text{ZrO}_2$  (YSZ) is columnar structures aligned along the build direction with elongated shape grains resulting from the blend of graphite

and YSZ (shown in Fig. 14(a)), and each column is subdivided into a stacks of grains with an elongated shape (shown in Fig. 14(b)) [26]. In another case, for the direct-SLS  $\text{SiC}$  ceramics prepared in medium energy density level, bonding was observed between the powder particles, and only surface melting and bonding occurred between the particles, with no apparent grain boundaries, as shown in Fig. 14(c) and (d). Particle clusters and needle-like protrusions parallel to the scanning direction are another feature of

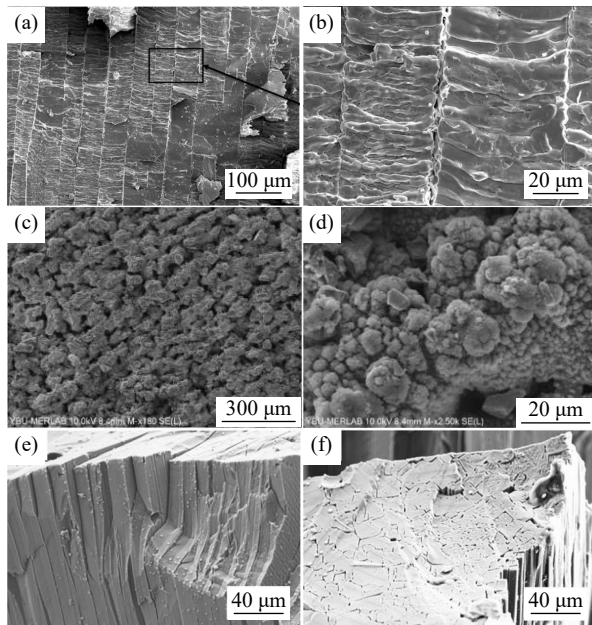


**Fig. 14.** Microstructure characteristics of  $\text{ZrO}_2$ ,  $\text{SiC}$ , and mullite fabricated by DLAM processes: (a, b) direct SLS  $\text{ZrO}_2$  ((a) along the build direction and (b) single column grain characteristics) [26]; (c, d) direct SLS  $\text{SiC}$  ((c) medium energy density level and (d) visible sintered particles) [27]; (e, f) LDED mullite ((e) middle of cylinder and (f) edge of cylinder) [61]. (a, b) Reprinted from *Addit. Manuf.*, 21, L. Ferrage, G. Bertrand, and P. Lenormand, Dense yttria-stabilized zirconia obtained by direct selective laser sintering, 472–478, Copyright 2018, with permission from Elsevier. (c, d) Reprinted from *Ceram. Int.*, 49, M. Abdelmoula, G. Küçüktürk, D. Grossin, A.M. Zarazaga, F. Maury, and M. Ferrato, Direct selective laser sintering of silicon carbide: Realizing the full potential through process parameter optimization, 32426–32439, Copyright 2023, with permission from Elsevier. (e, f) Reprinted by permission from Springer Nature: *J. Mater. Sci.*, *In situ* synthesis of melt-grown mullite ceramics using directed laser deposition, D.J. Wu, D.K. Zhao, F.Y. Niu, Y.F. Huang, J. Zhu, and G.Y. Ma, Copyright 2020.

SLS/SLM  $\text{SiC}$  ceramics when the powder binding mechanism is partially melting or not melting [92]. The SLS/SLM  $\text{Y}_2\text{O}_3$  ceramics also exhibit partial melting features with particle agglomeration, and the agglomerated particles are further sintered after the heat treatment under vacuum at a high temperature [29]. Furthermore, the microstructure of SLS/SLM  $\text{BaTiO}_3$  ceramics shows longer large grains with an average grain of 120  $\mu\text{m}$  and a secondary phase along the grain boundaries [30]. Other representatives of ceramics produced using the LDED processes are  $\text{MgAl}_2\text{O}_4$  and mullite. LDED  $\text{MgAl}_2\text{O}_4$  ceramics consist of the dark spinel phase ( $\text{MgAl}_2\text{O}_4$ ) and the light secondary phase ( $\text{MgO}\cdot 1.4\text{Al}_2\text{O}_3$ ) [40]. The average grain size of  $\text{MgAl}_2\text{O}_4$  gradually increases with increasing  $P$ . Another attractive ceramic is mullite, synthesized using high-purity  $\text{Al}_2\text{O}_3$  and  $\text{SiO}_2$  powders [61]. The microstructure of the LDED cylindrical mullite samples is characterized by central ‘tabular cellular’ and marginal ‘rod cellular,’ as shown in Fig. 14(e) and (f), with an over-evolution from the center to the edges, which is determined by the

difference in heat dissipation at different locations in the melt pool. The process parameters have an essential influence on the crystal structure of mullite [41].

## 5. Mechanical properties of DLAM ceramics

In this section, the mechanical properties of ceramics fabricated by the DLAM processes are recapitulated, with particular emphasis on relationships between process parameters, defects, microstructure, and properties, as well as the influence of external field assistance and post-treatment. The mechanical properties [5,25,35–37,39,42–43,46–48,50, 55–56,64,72,76–77,82,88,91] and enhancement methods [1,37,68,84,89,93–97] of DLAM ceramics are summarized in Tables 5 and 6, respectively.

### 5.1. Fracture toughness and microhardness

A key parameter associated with the serviceability and quality of ceramics is the fracture toughness ( $K_c$ ), which refers to their ability to resist crack propagation. Given the presence of defects such as microcracks and pores in DLAM ceramics with brittle and hard characteristics, evaluating and enhancing  $K_c$  is crucial for achieving high-quality ceramics through DLAM. The  $K_c$  of DLAM ceramics has been investigated on various ceramic materials, as listed in Table 5. Generally, the  $K_c$  of DLAM ceramics is comparable to or lower than that of conventionally sintered ceramics due to high-energy laser processing and strong crack sensitivity. The  $K_c$  is related to the intrinsic properties, microstructure, and defects of ceramics. Firstly, as described in previous sections, material compositing is one of the effective ways to tailor the microstructure directly, which can limit crack tip formation and further propagation. A typical representative is zirconia toughened alumina (ZTA) ceramics. DLAM ZTA ceramics can exhibit excellent  $K_c$  when changing material composition [43,46,87]. Notably, when the composition is a eutectic ratio, the nanoscale eutectic spacing significantly limits the crack propagation [82,94]. Moreover, the stress-induced volume increase caused by the  $\text{ZrO}_2$  phase transition ( $t\text{-ZrO}_2$  to  $m\text{-ZrO}_2$ ) is also a key factor for the increase in toughness in this material system. When the grain morphology of high-modulus strengthening phases ( $\text{ZrO}_2$  [87],  $\text{Al}_2\text{O}_3$  [5,56], and  $\text{SiC}$  [83]) changes from columnar crystals or columnar colonies to dendrites, the energy required for crack expansion increases, triggering the formation of toughening mechanisms such as crack deflection, branching, pinning, bridging, and microcracks. Secondly, by manipulating the thermal history of the DLAM processes [48], process optimization affects the solidification parameters ( $G$  and  $R$ ), which ultimately results in microstructure modulation to limit crack tip formation and further propagation. However, deposited parts are prone to cracking when the process parameters used exceed the threshold of laser energy density, while using too low laser energy density tends to form a melt pool with poor quality. Finally, as a method to affect thermal history and adjust microstructure, external field assistance is also a way to improve the properties of DLAM ceramics, such as ultra-

**Table 5.** Mechanical properties of ceramics fabricated by the DLAM processes

Material	Processes	P / W	v / (mm·min <sup>-1</sup> )	$\sigma_{fs}$ / MPa	$K_c$ / (MPa·m <sup>1/2</sup> )	$H_{Vickers}$ / GPa
Al <sub>2</sub> O <sub>3</sub> [64]	SLS/SLM	230	150	N/A	N/A	16.5 ± 1.1
Al <sub>2</sub> O <sub>3</sub> [25]	SLS/SLM	100–400	300–1000	N/A	N/A	16.3–18.3
Al <sub>2</sub> O <sub>3</sub> [37]	LDED	175	600	N/A	2.1 ± 1.3	15.2 ± 0.9
Al <sub>2</sub> O <sub>3</sub> [77]	LDED	375	300	210, 350 (max)	N/A	N/A
ZrO <sub>2</sub> [55]	SLS/SLM	30–90	0.6–12	N/A	N/A	11.4 ± 2.6
ZrO <sub>2</sub> [39]	LDED	250–350	355	N/A	N/A	19.1–19.8
Al <sub>2</sub> O <sub>3</sub> /ZrO <sub>2</sub> [82]	SLS/SLM	48–60	1200	173.8–538.1	6.2–9.1	14.9–15.4
Al <sub>2</sub> O <sub>3</sub> /ZrO <sub>2</sub> [78]	SLS/SLM	60	1200	>500	N/A	N/A
Al <sub>2</sub> O <sub>3</sub> /ZrO <sub>2</sub> [42]	LDED	410	400	N/A	4.79	16.8
Al <sub>2</sub> O <sub>3</sub> /ZrO <sub>2</sub> [72]	LDED	530	400	N/A	3.71 ± 0.3, 4.79 ± 0.3	17.15 ± 0.4
Al <sub>2</sub> O <sub>3</sub> /ZrO <sub>2</sub> [88]	LDED	300–450	300–450	N/A	6.52	18.59
Al <sub>2</sub> O <sub>3</sub> /ZrO <sub>2</sub> [46]	LDED	N/A	200	N/A	3.24–5.76	17.5–21.4
Al <sub>2</sub> O <sub>3</sub> /ZrO <sub>2</sub> [43]	LDED	350	600	N/A	2.63–3.64	14.4–18.5
Al <sub>2</sub> O <sub>3</sub> /ZrO <sub>2</sub> [47]	LDED	275	1000	103, 208	3.4, 3.8	16.5, 17.7
Al <sub>2</sub> O <sub>3</sub> /GdAlO <sub>3</sub> [35]	SLS/SLM	100–450	4–60	N/A	4.5 ± 0.1	17.1 ± 0.2
Al <sub>2</sub> O <sub>3</sub> /Al <sub>2</sub> TiO <sub>5</sub> [91]	LDED	250	400	~200–270	1.10–3.97	>1670
Al <sub>2</sub> O <sub>3</sub> /Al <sub>2</sub> TiO <sub>5</sub> [56]	LDED	250	50–900	~47.5–212	2.9–3.75	14.7–16.7
Al <sub>2</sub> O <sub>3</sub> /Al <sub>2</sub> TiO <sub>5</sub> [48]	LDED	150–350	300	142.59–227.41	3–3.87	13.7–15.7
Al <sub>2</sub> O <sub>3</sub> /mullite [5]	LDED	300	250	310.1 ± 36.5	CS: (2.00 ± 0.18)–(3.07 ± 0.13) LS: (1.95 ± 0.24)–(3.01 ± 0.18)	CS: (14.54 ± 0.23)–(18.39 ± 0.38) LS: 13.99 ± 0.11
Al <sub>2</sub> O <sub>3</sub> /Y <sub>3</sub> Al <sub>5</sub> O <sub>12</sub> /ZrO <sub>2</sub> [50]	LDED	220	558	N/A	CS: 3.53 ± 0.32 LS: 3.84 ± 0.44	CS: 20.6 ± 0.6 LS: 20.5 ± 0.6
Al <sub>2</sub> O <sub>3</sub> /GdAlO <sub>3</sub> /ZrO <sub>2</sub> [36]	SLS/SLM	200	6	N/A	6.1–7.8	14.3–15.3

Note: CS—Cross section; LS—Longitudinal section;  $\sigma_{fs}$ —Flexural strength;  $H_{Vickers}$ —Vickers microhardness.

sound-assistance [93–94] and water-cooling [89], as listed in Table 6. Due to the cavitation perturbation and mechanical stirring effects, a uniform and fine microstructure (nanoscale) of DLAM ceramics assisted by ultrasound [70] is beneficial for increasing  $K_c$ . Correspondingly, water-cooling of the substrate weakens the heat accumulation and significantly increases the cooling rate [89]. The microstructure of DLAM

ceramics transforms from a typical 3D network structure to a colony and dendrite structure with grain refinement, increasing  $K_c$ .

Because of its convenience, the indentation method is often used to measure the Vickers microhardness ( $H_{Vickers}$ ) of DLAM ceramics. The key elements that determine microhardness are crystal structure, density, grain orientation (e.g.,

**Table 6.** Mechanical properties of ceramic materials fabricated by DLAM processes under external field assistance and post-treatment

Material	Processes	Improvement of process	$\sigma_{fs}$ (Max <sup>#</sup> ) / MPa	$K_c$ (Max <sup>#</sup> ) / (MPa·m <sup>1/2</sup> )	$H_{Vickers}$ (Max <sup>#</sup> ) / GPa
Al <sub>2</sub> O <sub>3</sub> [37]	LDED	Heat treatment, 1000°C/5 h Heat treatment, 1600°C/5 h	N/A	4.4 ± 1.4 (109.52%)	16.66 ± 0.35 (9.25%)
Al <sub>2</sub> O <sub>3</sub> [1]	LDED	Heat treatment, 500–1600°C Heat treatment, 5–20 h	378.59–494.15 (83.00%) 471.04–547.85 (102.96%)	2.71–2.94 (3.16%) 2.84–3.07 (7.72%)	18.26–18.69 18.38–19.19
Al <sub>2</sub> O <sub>3</sub> + trace SiO <sub>2</sub> [95]	LDED	Heat treatment, 1000–1400°C/4 h	382.92–504.38 (62.65%)	3.09–3.54 (16.83%)	18.16–18.64 (2.47%)
Al <sub>2</sub> O <sub>3</sub> + TiC [96]	SLS/SLM	Heat treatment, 900°C/3 h	181, 232 (max)	N/A	N/A
Al <sub>2</sub> O <sub>3</sub> /GdAlO <sub>3</sub> /ZrO <sub>2</sub> [68]	LDED	Heat treatment, 1300–1500°C/200 h	N/A	3.69–4.04 (9.49%)	15.5–13.01 (−17.87%)
Al <sub>2</sub> O <sub>3</sub> /GdAlO <sub>3</sub> /ZrO <sub>2</sub> [97]	LDED	Heat treatment, 1200°C/1–8 h	N/A	3.40 ± 0.36 (−3.9%)	15.79 ± 0.44 (12.96%)
Al <sub>2</sub> O <sub>3</sub> /ZrO <sub>2</sub> [94]	LDED	Ultrasound-assisted, 20–160 W	N/A	7.67 ± 0.2 (17.64%)	16.22
Al <sub>2</sub> O <sub>3</sub> /ZrO <sub>2</sub> + C <sub>f</sub> [84]	LDED	Ultrasound-assisted, 120 W	N/A	8.7 ± 0.2 (33.44%)	N/A
Al <sub>2</sub> O <sub>3</sub> /ZrO <sub>2</sub> [93]	LDED	Ultrasound-assisted, 41 kHz, 5 μm*	N/A	N/A	17.15 (5.28%)
Al <sub>2</sub> O <sub>3</sub> /Y <sub>3</sub> Al <sub>5</sub> O <sub>12</sub> [89]	LDED	Water cooling assisted, 28°C	N/A	5.86 ± 1.11 (8.5%)	21.5 ± 2.7 (10.6%)

Note: \*—41 kHz is ultrasound frequency and 5 μm is ultrasound amplitude; Max<sup>#</sup>—Maximum change compared to as-fabricated, %.

texture), and grain size. The crystal structure depends on the atomic bonding of materials. Different ceramics exhibited different levels of microhardness values (Table 5). Density of ceramic materials is one of the most critical factors affecting the microhardness of SLS/SLM ceramics with solid sintering or partial melting. Increasing energy density and compacting powder bed contribute to densification, increasing microhardness. Because the microstructure of DLAM ceramics with full melting tends to grow epitaxially along the build direction, forming the columnar crystals, the microhardness tends to exhibit anisotropy with higher microhardness in the build direction than the scanning direction [5,50]. According to the Hall-Petch relationship, ceramics with small grain sizes possess high microhardness. Accordingly, controlling the process parameters, applying external fields to increase the  $G$  or  $R$  to reduce the grain size, and adding high-modulus reinforcing phases increase the microhardness of DLAM ceramics. For example, low  $Q$  leads to grain refinement and, as a result, increases the microhardness of SLS/SLM  $\text{Al}_2\text{O}_3$  ceramics [25]. After ultrasound assistance, LDED  $\text{Al}_2\text{O}_3/\text{ZrO}_2$  ceramics showed a significant increase in microhardness and wear resistance due to grain refinement [93].

## 5.2. Flexural strength

One of the prerequisites for using ceramic materials is that their flexural strength ( $\sigma_{fs}$ ) meets engineering requirements, especially when used as high-temperature structural material. Generally, the flexural strength of DLAM ceramics can reach the same order of magnitude as conventional sintering. For instance, a maximum value of 538.1 MPa for SLS/SLM  $\text{Al}_2\text{O}_3/\text{ZrO}_2$  composites [82], and 350 MPa for LDED  $\text{Al}_2\text{O}_3$  ceramics. However, the dispersion of strength values is relatively wide, which is related to the brittle fracture and the inhomogeneity defects of DLAM ceramics. For example, the average flexural strength value of LDED  $\text{Al}_2\text{O}_3$  is only 210 MPa [38], and that of the SLS/SLM  $\text{Al}_2\text{O}_3/\text{ZrO}_2$  composites is 208 MPa [47]. Hence, strength dispersion is an issue for DLAM ceramics. Further, according to the Hall-Petch relationship and the empirical relationship of strength/porosity [5], porosity and grain size seem to be two vital factors affecting the  $\sigma_{fs}$  of DLAM ceramic materials, and their relationship with strength is negatively correlated. The porosity of LDED  $\text{Al}_2\text{O}_3/\text{ZrO}_2$  composites decreases significantly when the  $Q$  increases, while the grain size may increase gradually [87]. Accordingly, Huang *et al.* [48] believes that the  $\sigma_{fs}$  usually shows a parabolic law that increases first and then decreases. The effect of microscopic defects on  $\sigma_{fs}$  seems not negligible considering the strength dispersion. The study [5] for DLAM  $\text{Al}_2\text{O}_3/\text{mullite}$  composites also found that the  $\sigma_{fs}$  of  $\text{Al}_2\text{O}_3$  ceramics was significantly enhanced (up to 310 MPa on average) with the addition of a small amount of  $\text{SiO}_2$  (3wt%), and the strengthening appeared to be due to the reduction of defects and residual stress, increase in the modulus, and change in the fracture pattern. However, the strength properties are still insufficient. Subsequent heat treatment of the DLAM parts may be a viable solution to further enhance the mechanical properties of DLAM ceramics

[95–96] due to residual stress relief, crack healing, and possibly grain size reduction.

## 6. Summary and outlook

Powder-based DLAM processes, which encompass powder beds and powder feeding, have sparked considerable excitement across various industries such as aerospace and energy. This excitement stems from their potential to manufacture ceramic parts with dense and intricate shapes in a single step. However, the development of DLAM for ceramics has been slower compared to metals and polymers. The fabrication of DLAM ceramics faces significant scientific and technological challenges, including the meticulous regulation and control of quality, defects, microstructures, and properties of DLAM ceramic parts. One major obstacle to the DLAM of high-performance ceramics, particularly concerning geometric and mechanical properties, is the inherent brittleness and low thermal shock tolerance juxtaposed with the need to withstand extremely high temperatures and repetitive thermal cycling. Recent publications on high-quality ceramics processed by DLAM provide considerable insights into potential trends in addressing these challenges, which are critical for the future development of DLAM ceramics. Fig. 15 illustrates some future perspectives on the development of DLAM ceramics.

(1) High-fidelity and high-efficiency numerical simulation and data-driven approach to support process optimization. There remains a significant gap between the geometric properties of DLAM ceramics and the actual requirements of various industries. Hence, optimizing different processing parameters becomes crucial for directly manufacturing high-performance ceramic parts, even though the process window for fabricating crack-free parts appears to be narrow. Numerical simulations of critical physical fields of the DLAM processes, such as temperature/stress and thermofluidic transport properties, may offer a viable solution for optimizing

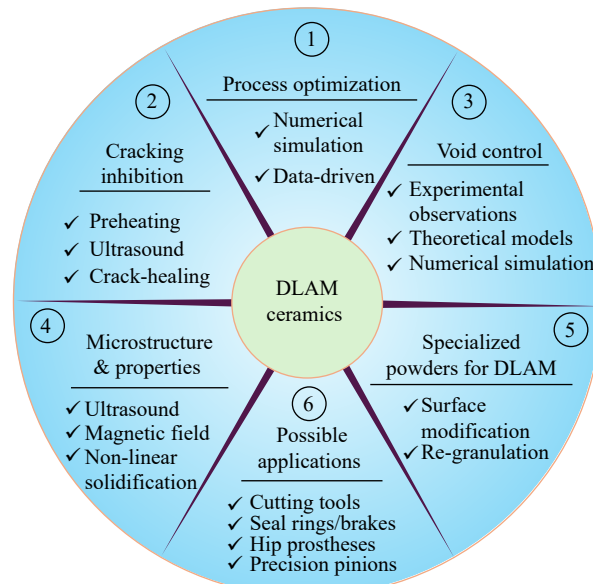


Fig. 15. Outlook and application of DLAM ceramics.

parameters and investigating process features of DLAM ceramics. The digital display of thermal history and stress distribution allows for a visualization of the metallurgical conditions, which in turn facilitates a deeper comprehension of defect formation. The revelation of the mass history of the shaping process provides the necessary guidance for the rational control of the melt pool geometrical characteristics, which contributes to the direct preparation of ceramic parts with superior geometrical properties. Build strategies based on a data-driven approach, such as machine learning, enables the direct optimization of process parameters based on part performance and enhances simulation efficiency. However, this approach necessitates the collection and analysis of substantial amounts of high-quality process data. Moreover, the challenge posed by extremely high process temperatures for data collection needs to be addressed. The development and application of online and real-time detection technologies show promise in overcoming this challenge.

(2) New crack initiation/propagation theory and inhibition strategy. Cracking is the primary restriction for DLAM of ceramic parts with large sectional dimensions. Preheating to assist the DLAM processes, such as DLAM Al<sub>2</sub>O<sub>3</sub>/ZrO<sub>2</sub>, is deemed advantageous for addressing this issue. Nonetheless, the effect of preheating, whether it pertains to the substrate or the ambient environment during the deposition process, on the metallurgical state of powder particles in the shaping process seems complicated to ignore. For instance, preheating can lead to worsened surface roughness of ceramic parts fabricated via the powder bed process. Introducing ultrasonic vibration can mitigate the tendency for cracking by enhancing the solidification environment of the melt pool and alleviating thermal stress through the uniform dispersion of materials. Nevertheless, the crack suppression effect appears to be limited and the surface roughness of the DLAM ceramic parts is poor. Directly observing fracture damage in brittle materials, particularly microcracking induced by thermal stress, is challenging. However, the speed of crack propagation seems to be influenced by the extent of material stretching at the crack tip front [98]. Therefore, inducing compressive stress at the crack front, such as through martensite phase transformation, timely material replenishment at the crack front, and filling crevasses, may offer effective solutions for inhibiting cracking in DLAM ceramics.

(3) New theory and approach for voids formation and control. Several investigations have demonstrated the feasibility of the DLAM processes in achieving ceramics with density close to 100%. However, achieving complete void elimination appears to be unattainable, particularly for materials with viscous properties like Si-based ceramics [28]. While analyzing gas solubility reduction and bubble movement in the melt pool can help understand the mechanism of pore formation. The unique metallurgical conditions involved in DLAM processes, such as high cooling rates, repetitive thermal cycling, and heat accumulation, contribute to a significantly complex pore formation mechanism compared to traditional processes like casting and welding. Consequently, further direct experi-

mental observations and theoretical models of the physical processes are essential to reduce the tendency of cracking caused by stress concentration in the voids. The development of online or offline observation methods for voids is expected to significantly advance our understanding of this issue. Furthermore, multi-physics field numerical simulation may be an effective tool to elucidate the motion laws of bubbles (such as dissolution, floating, merging, and growth under driving forces) during the shaping process, which determines the final shape of the voids in the ceramic parts.

(4) New approach to the control of microstructure and properties. The distinctive heat dissipation characteristic of DLAM ceramics often leads to a textured grain arrangement, such as epitaxial growth along the build direction, thereby resulting in anisotropic properties. The rapid solidification process, which causes an inhomogeneous microstructure distribution, leads to varying properties across different locations of the parts. Implementing field-assisted techniques, such as ultrasound or magnetic fields, to drive grain equiaxialization and nanosizing, can be potential solutions to counter thermally driven forces and the high entropy melting of ceramics. These approaches have the potential to significantly enhance the mechanical properties of DLAM ceramics. Furthermore, the shaping process of DLAM ceramics exhibits metallurgical features of non-equilibrium solidification. This is in contrast to the traditional solidification theory of local equilibrium at the interface, which fails to realistically reflect the actual solidification process. It may be possible to modulate the microstructure and mechanical properties by considering the non-linear solidification of the shaping process.

(5) Specialized ceramic powders suitable for DLAM. The raw powders currently used is primarily tailored for traditional industries on a large scale. However, given the unique process features of DLAM, developing specialized powders could serve as an alternative approach to manufacturing high-performance ceramics in a single step. This could involve designing and enhancing materials at the source, such as through re-granulation or surface modification of the raw ceramic powders. As an illustration, consider the mixing and spheroidisation of two ceramic powders with disparate thermophysical parameters, employing techniques such as sol-gel and plasma spheroidisation. Alternatively, a ceramic material exhibiting a negative expansion coefficient may be coated on the surface of the ceramic powders.

(6) Possible applications for DLAM ceramics. DLAM ceramics offer potential applications in specific small-sized bulk parts, such as precision cutting tools in mechanical manufacturing, automotive seal rings and brakes, hip prostheses for musculoskeletal hard connective tissues in dental, precision pinions for smart factories, and ceramic thermometry sensors that require subsequent processing. Additionally, the preparation of high-quality ceramic coatings presents an interesting application avenue. For instance, ceramic coatings produced using ultra-high-speed DLAM are expected to significantly enhance wear and corrosion resistance by reducing

cracking. However, there remains a significant disparity between the pressing demand for large-sized and complex-shaped parts across various industries and the current capabilities of DLAM processes in fabricating high-performance ceramics. This indicates that more efforts will be necessary to overcome these scientific and technical challenges in the future.

## Acknowledgements

The authors are grateful for the sponsorship of the following fund projects: the Guangdong Basic and Applied Basic Research Foundation, China (No. 2023A1515110578), the Guangzhou Basic and Applied Basic Research Project, China (No. 2024A04J00725), the Guangdong Academy of Sciences Project of Science and Technology Development, China (Nos. 2022GDASZH-2022010107 and 2022GDASZH-2022010108). Dr. Zhao would particularly like to thank his wife, M.S. Guo, for her help with the language of the manuscript and for the encouragement of their newborn baby.

## Conflict of Interest

Guijun Bi is an editorial board member for this journal and was not involved in the editorial review or the decision to publish this article. All authors state that there is no conflict of interest.

## References

- [1] D.K. Zhao, G.J. Bi, J. Chen, *et al.*, Melt-grown behaviour of heat treated high-purity alumina ceramics prepared by laser directed energy deposition, *Ceram. Int.*, 50(2024), No. 1, p. 1777.
- [2] B.K. Yıldız, H. Yılmaz, and Y.K. Tür, Influence of nickel addition on the microstructure and mechanical properties of  $\text{Al}_2\text{O}_3$ -5vol% $\text{ZrO}_2$  ceramic composites prepared via precipitation method, *Int. J. Miner. Metall. Mater.*, 26(2019), No. 7, p. 908.
- [3] J.X. Wen, T.B. Zhu, Z.P. Xie, W.B. Cao, and W. Liu, A strategy to obtain a high-density and high-strength zirconia ceramic *via* ceramic injection molding by the modification of oleic acid, *Int. J. Miner. Metall. Mater.*, 24(2017), No. 6, p. 718.
- [4] R.Y. Su, J.Y. Chen, X.Q. Zhang, *et al.*, Accuracy controlling and mechanical behaviors of precursor-derived ceramic SiOC microlattices by projection micro stereolithography ( $\mu$ SL) 3D printing, *J. Adv. Ceram.*, 12(2023), No. 11, p. 2134.
- [5] D.K. Zhao, D.J. Wu, J. Shi, F.Y. Niu, and G.Y. Ma, Microstructure and mechanical properties of melt-grown alumina-mullite/glass composites fabricated by directed laser deposition, *J. Adv. Ceram.*, 11(2022), No. 1, p. 75.
- [6] N.P. Padture, Advanced structural ceramics in aerospace propulsion, *Nat. Mater.*, 15(2016), p. 804.
- [7] S.J. Zinkle and G.S. Was, Materials challenges in nuclear energy, *Acta Mater.*, 61(2013), No. 3, p. 735.
- [8] C.L. Cramer, E. Ionescu, M. Graczyk-Zajac, *et al.*, Additive manufacturing of ceramic materials for energy applications: Road map and opportunities, *J. Eur. Ceram. Soc.*, 42(2022), No. 7, p. 3049.
- [9] K.P. Misra and R.D.K. Misra, Advanced ceramics, [in] K.P. Misra and R.D.K. Misra, eds., *Ceramic Science and Engineering*, Elsevier, Amsterdam, 2022, p. 21.
- [10] P.X. Zhang, E.H. Wang, J.J. Liu, T. Yang, H.L. Wang, and X.M. Hou, Porous high-entropy rare-earth phosphate (REPO<sub>4</sub>, RE = La, Sm, Eu, Ce, Pr and Gd) ceramics with excellent thermal insulation performance *via* pore structure tailoring, *Int. J. Miner. Metall. Mater.*, 31(2024), No. 7, p. 1651.
- [11] M. Rodchom, P. Wimuktiwan, K. Soongprasit, D. Atong, and S. Vichaphund, Preparation and characterization of ceramic materials with low thermal conductivity and high strength using high-calcium fly ash, *Int. J. Miner. Metall. Mater.*, 29(2022), No. 8, p. 1635.
- [12] M.H. Zhang, B.C. Zhang, Y.J. Wen, and X.H. Qu, Research progress on selective laser melting processing for nickel-based superalloy, *Int. J. Miner. Metall. Mater.*, 29(2022), No. 3, p. 369.
- [13] X.Q. Zhang, K.Q. Zhang, B. Zhang, Y. Li, and R.J. He, Mechanical properties of additively-manufactured cellular ceramic structures: A comprehensive study, *J. Adv. Ceram.*, 11(2022), No. 12, p. 1918.
- [14] X.K. Zhao and X.S. Hai, Microstructure and tribological behavior of the nickel-coated-graphite-reinforced Babbitt metal composite fabricated via selective laser melting, *Int. J. Miner. Metall. Mater.*, 29(2022), No. 2, p. 320.
- [15] Y.L. Lin, D. Wang, C. Yang, W.W. Zhang, and Z. Wang, An Al-Al interpenetrating-phase composite by 3D printing and hot extrusion, *Int. J. Miner. Metall. Mater.*, 30(2023), No. 4, p. 678.
- [16] K.Q. Zhang, Q.Y. Meng, Z.L. Qu, and R.J. He, A review of defects in vat photopolymerization additive-manufactured ceramics: Characterization, control, and challenges, *J. Eur. Ceram. Soc.*, 44(2024), No. 3, p. 1361.
- [17] Y.B. Shan, Y. Bai, S. Yang, *et al.*, 3D-printed strontium-incorporated  $\beta$ -TCP bioceramic triply periodic minimal surface scaffolds with simultaneous high porosity, enhanced strength, and excellent bioactivity, *J. Adv. Ceram.*, 12(2023), No. 9, p. 1671.
- [18] W. Zheng, J.M. Wu, S. Chen, *et al.*, Influence of  $\text{Al}_2\text{O}_3$  content on mechanical properties of silica-based ceramic cores prepared by stereolithography, *J. Adv. Ceram.*, 10(2021), No. 6, p. 1381.
- [19] M. Schmidt, M. Merklein, D. Bourell, *et al.*, Laser based additive manufacturing in industry and academia, *CIRP Ann.*, 66(2017), No. 2, p. 561.
- [20] S. Dadhania, 3D Printing Ceramics 2022–2032: Technology and Market Outlook, 2022 [2023-11-26]. <https://www.idtechex.com/en/research-report/3d-printing-ceramics-2022-2032-technology-and-market-outlook/834>
- [21] S. Pfeiffer, K. Florio, D. Puccio, *et al.*, Direct laser additive manufacturing of high performance oxide ceramics: A state-of-the-art review, *J. Eur. Ceram. Soc.*, 41(2021), No. 13, p. 6087.
- [22] Y. Lakhdar, C. Tuck, J. Binner, A. Terry, and R. Goodridge, Additive manufacturing of advanced ceramic materials, *Prog. Mater. Sci.*, 116(2021), art. No. 100736.
- [23] Z.Q. Fan, Q.Y. Tan, C.W. Kang, and H. Huang, Advances and challenges in direct additive manufacturing of dense ceramic oxides, *Int. J. Extreme Manuf.*, 6(2024), No. 5, art. No. 052004.
- [24] E. Juste, F. Petit, V. Lardot, and F. Cambier, Shaping of ceramic parts by selective laser melting of powder bed, *J. Mater. Res.*, 29(2014), No. 17, p. 2086.
- [25] Z.Q. Fan, M.Y. Lu, and H. Huang, Selective laser melting of alumina: A single track study, *Ceram. Int.*, 44(2018), No. 8, p. 9484.
- [26] L. Ferrage, G. Bertrand, and P. Lenormand, Dense yttria-stabilized zirconia obtained by direct selective laser sintering, *Addit. Manuf.*, 21(2018), p. 472.
- [27] M. Abdelmoula, G. Küçüktürk, D. Grossin, A.M. Zarazaga, F. Maury, and M. Ferrato, Direct selective laser sintering of silicon carbide: Realizing the full potential through process parameter optimization, *Ceram. Int.*, 49(2023), No. 20, p. 32426.
- [28] K.C. Datsiou, E. Saleh, F. Spirrett, R. Goodridge, I. Ashcroft, and D. Eustice, Additive manufacturing of glass with laser powder bed fusion, *J. Am. Ceram. Soc.*, 102(2019), No. 8, p.

- 4410.
- [29] A. Ratsimba, A. Zerrouki, N. Tessier-Doyen, et al., Densification behaviour and three-dimensional printing of  $\text{Y}_2\text{O}_3$  ceramic powder by selective laser sintering, *Ceram. Int.*, 47(2021), No. 6, p. 7465.
  - [30] X. Zhang, F. Wang, Z.P. Wu, et al., Direct selective laser sintering of hexagonal barium titanate ceramics, *J. Am. Ceram. Soc.*, 104(2021), No. 3, p. 1271.
  - [31] X. Zhang, N. Li, X. Chen, M. Stroup, Y.F. Lu, and B. Cui, Direct selective laser sintering of high-entropy carbide ceramics, *J. Mater. Res.*, 38(2023), No. 1, p. 187.
  - [32] J. Wilkes, Y.C. Hagedorn, W. Meiners, and K. Wissenbach, Additive manufacturing of  $\text{ZrO}_2\text{-Al}_2\text{O}_3$  ceramic components by selective laser melting, *Rapid Prototyping J.*, 19(2013), No. 1, p. 51.
  - [33] F. Verga, M. Borlaf, L. Conti, et al., Laser-based powder bed fusion of alumina toughened zirconia, *Addit. Manuf.*, 31(2020), art. No. 100959.
  - [34] Y. Zhang, K. Zhang, D. Chen, et al., Morphology and formation mechanism of cracks in  $\text{Al}_2\text{O}_3\text{-ZrO}_2$  eutectic ceramics fabricated via laser powder bed fusion, *J. Am. Ceram. Soc.*, 107(2024), No. 4, p. 2128.
  - [35] Z.L. Shen, H.J. Su, H.F. Liu, et al., Directly fabricated  $\text{Al}_2\text{O}_3\text{/GdAlO}_3$  eutectic ceramic with large smooth surface by selective laser melting: Rapid solidification behavior and thermal field simulation, *J. Eur. Ceram. Soc.*, 42(2022), No. 3, p. 1088.
  - [36] H.F. Liu, H.J. Su, Z.L. Shen, et al., Direct formation of  $\text{Al}_2\text{O}_3\text{/GdAlO}_3\text{/ZrO}_2$  ternary eutectic ceramics by selective laser melting: Microstructure evolutions, *J. Eur. Ceram. Soc.*, 38(2018), No. 15, p. 5144.
  - [37] V.K. Balla, S. Bose, and A. Bandyopadhyay, Processing of bulk alumina ceramics using laser engineered net shaping, *Int. J. Appl. Ceram. Technol.*, 5(2008), No. 3, p. 234.
  - [38] F.Y. Niu, D.J. Wu, F. Lu, G. Liu, G.Y. Ma, and Z.Y. Jia, Microstructure and macro properties of  $\text{Al}_2\text{O}_3$  ceramics prepared by laser engineered net shaping, *Ceram. Int.*, 44(2018), No. 12, p. 14303.
  - [39] Z.Q. Fan, Y.T. Zhao, M.Y. Lu, and H. Huang, Yttria stabilized zirconia (YSZ) thin wall structures fabricated using laser engineered net shaping (LENS), *Int. J. Adv. Manuf. Technol.*, 105(2019), No. 11, p. 4491.
  - [40] J.M. Pappas, A.R. Thakur, E.C. Kinzel, and X.Y. Dong, Direct 3D printing of transparent magnesium aluminate spinel ceramics, *J. Laser Appl.*, 33(2021), No. 1, art. No. 012018.
  - [41] D.J. Wu, D.K. Zhao, Y.F. Huang, F.Y. Niu, and G.Y. Ma, Shaping quality, microstructure, and mechanical properties of melt-grown mullite ceramics by directed laser deposition, *J. Alloys Compd.*, 871(2021), art. No. 159609.
  - [42] F.Y. Niu, D.J. Wu, G.Y. Ma, J.T. Wang, M.H. Guo, and B. Zhang, Nanosized microstructure of  $\text{Al}_2\text{O}_3\text{-ZrO}_2$  ( $\text{Y}_2\text{O}_3$ ) eutectics fabricated by laser engineered net shaping, *Scripta Mater.*, 95(2015), p. 39.
  - [43] Y.B. Hu, H. Wang, W.L. Cong, and B. Zhao, Directed energy deposition of zirconia-toughened alumina ceramic: Novel microstructure formation and mechanical performance, *J. Manuf. Sci. Eng.*, 142(2020), No. 2, art. No. 021005.
  - [44] Z.Q. Fan, Y. Yin, Q.Y. Tan, et al., Unveiling solidification mode transition and crystallographic characteristics in laser 3D-printed  $\text{Al}_2\text{O}_3\text{-ZrO}_2$  eutectic ceramics, *Scripta Mater.*, 210(2022), art. No. 114433.
  - [45] S. Yan, Y.F. Huang, D.K. Zhao, F.Y. Niu, G.Y. Ma, and D.J. Wu, 3D printing of nano-scale  $\text{Al}_2\text{O}_3\text{-ZrO}_2$  eutectic ceramic: Principle analysis and process optimization of pores, *Addit. Manuf.*, 28(2019), p. 120.
  - [46] F.Z. Li, X.W. Zhang, C.Y. Sui, J.Z. Wu, H.Y. Wei, and Y. Zhang, Microstructure and mechanical properties of  $\text{Al}_2\text{O}_3\text{-ZrO}_2$  ceramic deposited by laser direct material deposition, *Ceram. Int.*, 44(2018), No. 15, p. 18960.
  - [47] J.M. Pappas, A.R. Thakur, and X.Y. Dong, Effects of zirconia doping on additively manufactured alumina ceramics by laser direct deposition, *Mater. Des.*, 192(2020), art. No. 108711.
  - [48] Y.F. Huang, D.J. Wu, D.K. Zhao, F.Y. Niu, and G.Y. Ma, Investigation of melt-growth alumina/aluminum titanate composite ceramics prepared by directed energy deposition, *Int. J. Extreme Manuf.*, 3(2021), No. 3, art. No. 035101.
  - [49] H.J. Su, H.F. Liu, H. Jiang, et al., One-step preparation of melt-grown  $\text{Al}_2\text{O}_3\text{/GdAlO}_3\text{/ZrO}_2$  eutectic ceramics with large size and irregular shape by directed energy deposition, *Addit. Manuf.*, 70(2023), art. No. 103563.
  - [50] Z.Q. Fan, Y.T. Zhao, Q.Y. Tan, et al., Nanostructured  $\text{Al}_2\text{O}_3\text{-YAG-ZrO}_2$  ternary eutectic components prepared by laser engineered net shaping, *Acta Mater.*, 170(2019), p. 24.
  - [51] Z.Q. Fan, Y.T. Zhao, Q.Y. Tan, B.W. Yu, M.X. Zhang, and H. Huang, New insights into the growth mechanism of 3D-printed  $\text{Al}_2\text{O}_3\text{-Y}_3\text{Al}_5\text{O}_{12}$  binary eutectic composites, *Scripta Mater.*, 178(2020), p. 274.
  - [52] Y.D. Qiu, J.M. Wu, A.N. Chen, et al., Balling phenomenon and cracks in alumina ceramics prepared by direct selective laser melting assisted with pressure treatment, *Ceram. Int.*, 46(2020), No. 9, p. 13854.
  - [53] D.J. Wu, J.D. San, F.Y. Niu, et al., Effect and mechanism of  $\text{ZrO}_2$  doping on the cracking behavior of melt-grown  $\text{Al}_2\text{O}_3$  ceramics prepared by directed laser deposition, *Int. J. Appl. Ceram. Technol.*, 17(2020), No. 1, p. 227.
  - [54] A. Montón Zarazaga, M. Abdelmoula, G. Küçüktürk, F. Maury, M. Ferrato, and D. Grossin, Process parameters investigation for direct powder bed selective laser processing of silicon carbide parts, *Prog. Addit. Manuf.*, 7(2022), No. 6, p. 1307.
  - [55] Q. Liu, B. Song, and H.L. Liao, Microstructure study on selective laser melting yttria stabilized zirconia ceramic with near IR fiber laser, *Rapid Prototyping J.*, 20(2014), No. 5, p. 346.
  - [56] Y.F. Huang, D.J. Wu, D.K. Zhao, et al., Process optimization of melt growth alumina/aluminum titanate composites directed energy deposition: Effects of scanning speed, *Addit. Manuf.*, 35(2020), art. No. 101210.
  - [57] Z.L. Shen, H.J. Su, M.H. Yu, et al., Large-size complex-structure ternary eutectic ceramic fabricated using laser powder bed fusion assisted with finite element analysis, *Addit. Manuf.*, 72(2023), art. No. 103627.
  - [58] P. Bertrand, F. Bayle, C. Combe, P. Goeuriot, and I. Smurov, Ceramic components manufacturing by selective laser sintering, *Appl. Surf. Sci.*, 254(2007), No. 4, p. 989.
  - [59] I. Shishkovsky, I. Yadroitsev, P. Bertrand, and I. Smurov, Alumina-zirconium ceramics synthesis by selective laser sintering/melting, *Appl. Surf. Sci.*, 254(2007), No. 4, p. 966.
  - [60] Y.Z. Li, Y.B. Hu, W.L. Cong, L. Zhi, and Z.N. Guo, Additive manufacturing of alumina using laser engineered net shaping: Effects of deposition variables, *Ceram. Int.*, 43(2017), No. 10, p. 7768.
  - [61] D.J. Wu, D.K. Zhao, F.Y. Niu, Y.F. Huang, J. Zhu, and G.Y. Ma, *In situ* synthesis of melt-grown mullite ceramics using directed laser deposition, *J. Mater. Sci.*, 55(2020), No. 27, p. 12761.
  - [62] S.Q. Ma, Y.Q. Jiang, S. Fu, et al., 3D-printed Lunar regolith simulant-based geopolymer composites with bio-inspired sandwich architectures, *J. Adv. Ceram.*, 12(2023), No. 3, p. 510.
  - [63] Y. Tang, J.Y.H. Fuh, H.T. Loh, Y.S. Wong, and L. Lu, Direct laser sintering of a silica sand, *Mater. Des.*, 24(2003), No. 8, p. 623.
  - [64] E.M. Fayed, A.S. Elmesalamy, M. Sobih, and Y. Elshaer, Characterization of direct selective laser sintering of alumina, *Int. J. Adv. Manuf. Technol.*, 94(2018), No. 5, p. 2333.
  - [65] Y.C. Hagedorn, N. Balachandran, W. Meiners, K. Wissenbach, and R. Poprawe, SLM of net-shaped high strength ceramics: new opportunities for producing dental restorations, [in] *Pro-*

- ceedings for the 2011 International Solid Freeform Fabrication Symposium, Austin, 2011, p. 8.
- [66] M. Abdelmoula, G. Küçüktürk, E. Juste, and F. Petit, Powder bed selective laser processing of alumina: Scanning strategies investigation, *Appl. Sci.*, 12(2022), No. 2, art. No. 764.
- [67] Z.W. Xiong, K. Zhang, Z.G. Zhu, *et al.*, Effect of laser focus shift on the forming quality, microstructure and mechanical properties of additively manufactured  $\text{Al}_2\text{O}_3$ – $\text{ZrO}_2$  eutectic ceramics, *Ceram. Int.*, 49(2023), No. 22, p. 35948.
- [68] H.F. Liu, H.J. Su, Z.L. Shen, *et al.*, Insights into high thermal stability of laser additively manufactured  $\text{Al}_2\text{O}_3$ / $\text{GdAlO}_3$ / $\text{ZrO}_2$  eutectic ceramics under high temperatures, *Addit. Manuf.*, 48(2021), Part B, art. No. 102425.
- [69] G.K. Mishra, C.P. Paul, A.K. Rai, A.K. Agrawal, S.K. Rai, and K.S. Bindra, Experimental investigation on laser directed energy deposition based additive manufacturing of  $\text{Al}_2\text{O}_3$  bulk structures, *Ceram. Int.*, 47(2021), No. 4, p. 5708.
- [70] J. Deckers, S. Meyers, J.P. Kruth, and J. Vleugels, Direct selective laser sintering/melting of high density alumina powder layers at elevated temperatures, *Physics Procedia*, 56(2014), p. 117.
- [71] Q. Liu, Y. Danlos, B. Song, B.C. Zhang, S. Yin, and H.L. Liao, Effect of high-temperature preheating on the selective laser melting of yttria-stabilized zirconia ceramic, *J. Mater. Process. Technol.*, 222(2015), p. 61.
- [72] G.Y. Ma, S. Yan, F.Y. Niu, Y.L. Zhang, and D.J. Wu, Microstructure and mechanical properties of solid  $\text{Al}_2\text{O}_3$ – $\text{ZrO}_2$  ( $\text{Y}_2\text{O}_3$ ) eutectics prepared by laser engineered net shaping, *J. Laser Appl.*, 29(2017), No. 2, art. No. 022305.
- [73] S. Yan, D.J. Wu, F.Y. Niu, Y.F. Huang, N. Liu, and G.Y. Ma, Effect of ultrasonic power on forming quality of nano-sized  $\text{Al}_2\text{O}_3$ – $\text{ZrO}_2$  eutectic ceramic via laser engineered net shaping (LENS), *Ceram. Int.*, 44(2018), No. 1, p. 1120.
- [74] H.F. Liu, H.J. Su, Z.L. Shen, *et al.*, One-step additive manufacturing and microstructure evolution of melt-grown  $\text{Al}_2\text{O}_3$ / $\text{GdAlO}_3$ / $\text{ZrO}_2$  eutectic ceramics by laser directed energy deposition, *J. Eur. Ceram. Soc.*, 41(2021), No. 6, p. 3547.
- [75] Y. Zheng, K. Zhang, T.T. Liu, W.H. Liao, C.D. Zhang, and H. Shao, Cracks of alumina ceramics by selective laser melting, *Ceram. Int.*, 45(2019), No. 1, p. 175.
- [76] H. Yves-Christian, W. Jan, M. Wilhelm, W. Konrad, and P. Reinhart, Net shaped high performance oxide ceramic parts by selective laser melting, *Physics Procedia*, 5(2010), p. 587.
- [77] F.Y. Niu, D.J. Wu, S. Yan, G.Y. Ma, and B. Zhang, Process optimization for suppressing cracks in laser engineered net shaping of  $\text{Al}_2\text{O}_3$  ceramics, *JOM*, 69(2017), No. 3, p. 557.
- [78] Z.W. Liu, C.B. Ma, Z.X. Chang, *et al.*, Formation mechanism and quantitative analysis of pores in  $\text{Al}_2\text{O}_3$ – $\text{ZrO}_2$  ceramic different structures by laser additive manufacturing, *Ceram. Int.*, 49(2023), No. 10, p. 16099.
- [79] Y.H. Wang, Q.R. Zhang, H.B. Zhang, and J.C. Lei, Deep-learning-based localized porosity analysis for laser-sintered  $\text{Al}_2\text{O}_3$  ceramic paste, *Ceram. Int.*, 49(2023), No. 14, p. 23426.
- [80] Z. Liu, K. Song, B. Gao, *et al.*, Microstructure and mechanical properties of  $\text{Al}_2\text{O}_3$ / $\text{ZrO}_2$  directionally solidified eutectic ceramic prepared by laser 3D printing, *J. Mater. Sci. Technol.*, 32(2016), No. 4, p. 320.
- [81] S. Buls, J. Vleugels, and B. Van Hooreweder, Microwave assisted selective laser melting of technical ceramics, [in] *Proceedings of the 29th Annual International Solid Freeform Fabrication Symposium—An Additive Manufacturing Conference*, Austin, 2018, p. 2349.
- [82] J. Wilkes, *Selective Laser Melting for Generative Production of Components from High-Strength Oxide Ceramics (in Germany)* [Dissertation], RWTH Aachen University, Aachen, 2009.
- [83] D.J. Wu, F. Lu, D.K. Zhao, *et al.*, Effect of doping  $\text{SiC}$  particles on cracks and pores of  $\text{Al}_2\text{O}_3$ – $\text{ZrO}_2$  eutectic ceramics fabricated by directed laser deposition, *J. Mater. Sci.*, 54(2019), No. 13, p. 9321.
- [84] S. Yan, D.J. Wu, Y.F. Huang, *et al.*, C fiber toughening  $\text{Al}_2\text{O}_3$ – $\text{ZrO}_2$  eutectic via ultrasonic-assisted directed laser deposition, *Mater. Lett.*, 235(2019), p. 228.
- [85] S.M. Hashemi, S. Parvizi, H. Baghbanjavid, *et al.*, Computational modelling of process–structure–property–performance relationships in metal additive manufacturing: A review, *Int. Mater. Rev.*, 67(2022), No. 1, p. 1.
- [86] S. Pfeiffer, M. Makowska, K. Florio, *et al.*, Selective laser melting of thermal pre-treated metal oxide doped aluminum oxide granules, *Open Ceram.*, 2(2020), art. No. 100007.
- [87] D.J. Wu, J.D. San, F.Y. Niu, D.K. Zhao, Y.F. Huang, and G.Y. Ma, Directed laser deposition of  $\text{Al}_2\text{O}_3$ – $\text{ZrO}_2$  melt-grown composite ceramics with multiple composition ratios, *J. Mater. Sci.*, 55(2020), No. 16, p. 6794.
- [88] S. Yan, D.J. Wu, G.Y. Ma, F.Y. Niu, R.K. Kang, and D.M. Guo, Formation mechanism and process optimization of nano  $\text{Al}_2\text{O}_3$ – $\text{ZrO}_2$  eutectic ceramic via laser engineered net shaping (LENS), *Ceram. Int.*, 43(2017), No. 17, p. 14742.
- [89] D.J. Wu, H.C. Liu, F. Lu, *et al.*,  $\text{Al}_2\text{O}_3$ –YAG eutectic ceramic prepared by laser additive manufacturing with water-cooled substrate, *Ceram. Int.*, 45(2019), No. 3, p. 4119.
- [90] H.F. Liu, H.J. Su, Z.L. Shen, *et al.*, Preparation of large-size  $\text{Al}_2\text{O}_3$ / $\text{GdAlO}_3$ / $\text{ZrO}_2$  ternary eutectic ceramic rod by laser directed energy deposition and its microstructure homogenization mechanism, *J. Mater. Sci. Technol.*, 85(2021), p. 218.
- [91] D.J. Wu, Y.F. Huang, F.Y. Niu, *et al.*, Effects of  $\text{TiO}_2$  doping on microstructure and properties of directed laser deposition alumina/aluminum titanate composites, *Virtual Phys. Prototyping*, 14(2019), No. 4, p. 371.
- [92] A. Montón, M. Abdelmoula, G. Küçüktürk, F. Maury, D. Grossin, and M. Ferrato, Experimental and numerical study for direct powder bed selective laser processing (sintering/melting) of silicon carbide ceramic, *Mater. Res. Express*, 8(2021), No. 4, art. No. 045603.
- [93] Y.B. Hu, F.D. Ning, W.L. Cong, Y.C. Li, X.L. Wang, and H. Wang, Ultrasonic vibration-assisted laser engineering net shaping of  $\text{ZrO}_2$ – $\text{Al}_2\text{O}_3$  bulk parts: Effects on crack suppression, microstructure, and mechanical properties, *Ceram. Int.*, 44(2018), No. 3, p. 2752.
- [94] S. Yan, D.J. Wu, F.Y. Niu, G.Y. Ma, and R.K. Kang,  $\text{Al}_2\text{O}_3$ – $\text{ZrO}_2$  eutectic ceramic via ultrasonic-assisted laser engineered net shaping, *Ceram. Int.*, 43(2017), No. 17, p. 15905.
- [95] D.K. Zhao, D.J. Wu, F.Y. Niu, *et al.*, Heat treatment of melt-grown alumina ceramics with trace glass fabricated by laser directed energy deposition, *Mater. Charact.*, 196(2023), art. No. 112639.
- [96] F. Verga, M. Makowska, G. Cellerai, K. Florio, M. Schmid, and K. Wegener, Crack-healing, a novel approach for a laser-based powder bed fusion of high-performance ceramic oxides, *Addit. Manuf. Lett.*, 1(2021), art. No. 100021.
- [97] H.F. Liu, H.J. Su, Z.L. Shen, *et al.*, Formation mechanism and roles of oxygen vacancies in melt-grown  $\text{Al}_2\text{O}_3$ / $\text{GdAlO}_3$ / $\text{ZrO}_2$  eutectic ceramic by laser 3D printing, *J. Adv. Ceram.*, 11(2022), No. 11, p. 1751.
- [98] M. Wang, S. Shi, and J. Fineberg, Tensile cracks can shatter classical speed limits, *Science*, 381(2023), No. 6656, p. 415.